

AD-A285 609



V PAGE Dist: A

Form Approved
OMB No. 0704-0188

Use per response, including the time for reviewing instructions, searching existing data sources, gathering and maintaining the data needed, and completing and reviewing the collection of information. Send comments regarding this burden estimate or any other aspect of this plan to Headquarters Services, Directorate for Information Operations and Reports, 1215 Jefferson Davis and Budget, Paperwork Reduction Project (0704-0188), Washington, DC 20503.

3. REPORT TYPE AND DATES COVERED

August 1994

Final

4/1/92-8/31/94

4. TITLE AND SUBTITLE

Study of Improved Critical Currents and
Mechanical Properties in YBaCuO
Superconductor w/Ag or 211 Dispersions

6. AUTHOR(S)

Siu-Wai Chan

5. FUNDING NUMBERS

G F49620-92-J-
0160

7. PERFORMING ORGANIZATION NAME(S) AND ADDRESS(ES)

The Trustees of Columbia University in
The City of New York, New York, NY 10027

8. PERFORMING ORGANIZATION
REPORT NUMBER

1

AFOSR-TR 94 0651

9. SPONSORING/MONITORING AGENCY NAME(S) AND ADDRESS(ES)

AFOSR NE
Bolling AFB, DC 20332-0001

SPONSORING/MONITORING
AGENCY REPORT NUMBER

1

11. SUPPLEMENTARY NOTES

12a. DISTRIBUTION/AVAILABILITY STATEMENT

Unlimited approved for public release;
distribution unlimited.

12b. DISTRIBUTION CODE

A

13. ABSTRACT (Maximum 200 words) The microstructure of the top-seeded, single grain, melted textured YBCO materials with different vol% 211 were investigated. The homogeneity of 211 distribution was greatly improved by using a solution precipitated 211 powder in preparation. Crack spacings and twin spacings were found to decrease with increasing vol% of the 211 particles. The 211 particles were found to be effective in holding crack propagation. Relationship between twin spacing and interparticle spacing was found to depend on the elastic strain energy from the tetragonal to orthorhombic transformation. The accumulative beneficial effects of the 211 addition on J_c are summarized. The highest J_c was 10^4 A/cm² at 77K 1T.

Our transmission electron microscopy of the Au/ YBCO interfaces shows well-bonded interfaces with no extraneous phases present with the (001) lattice fringe of YBCO terminated at the interfaces abruptly. Both integral steps of [001] height and multiples of 1/3[001] steps were observed. Our finding supports earlier contact resistivity and XPS results of the Au/YBCO interfaces.

Amorphous carbon films were shown to protect superconducting YBCO films from degradation by humidity. The YBCO films with carbon coating were found to retain critical current densities 4 orders of magnitude higher than the uncoated YBCO films after 2h at 100% relative humidity stressing at room temperature.

14. SUBJECT TERMS

Superconductors, Critical Currents, Flux-pinning
Dispersion, Passivation, Thin Films, Twins

15. NUMBER OF PAGES

93

16. PRICE CODE

17. SECURITY CLASSIFICATION
OF REPORT

Unclassified

18. SECURITY CLASSIFICATION
OF THIS PAGE

Unclassified

19. SECURITY CLASSIFICATION
OF ABSTRACT

Unclassified

20. LIMITATION OF ABSTRACT

UL

NSN 7540-01-280-5500

Standard Form 298 (Rev. 2-89)
Prescribed by ANSI Std Z39-18
298-102

53-85

DTIC QUALITY INVESTIGATED 3

TECHNICAL REPORT 4/1/92-8/31/94

Study of Improved Critical Currents and Mechanical Properties in
The Y-Ba-Cu-O Superconductor with Silver or Y_2BaCuO_3 (211)
Dispersions

STATEMENT OF WORK

The melted textured bulk materials of YBCO with different vol% 211 from Dr. Jin of AT&T were thoroughly investigated. Since the microstructures were of extremely large scale, optical microscopy was first employed and followed by scanning electron microscopy.

Findings from Jin's samples include:

- (1) The local density of 211 particles affect the local surface cracks distribution.
- (2) 211 particles are effective crack blunters.

We have also investigated a set of large grained YBCO materials with 10, 20, 30, 40, and 50 211 vol% from Dr. Ruling Meng. The 211 particles were prepared from controlled precipitations which gave a finer particle size and a tight control of particle size distribution. These YBCO materials were much more homogenous under optical microscope and often scanning electron microscopy and transmission electron microscopy were employed. We have looked for a correlation among the twin spacing, the spacing of the surface (001) cracks, and the measured J_c as the 211 amount varies.

Findings from this set of samples are:

- (1) Crack spacing tracks with the vol% of 211. The spacing are 8, 5, 3 μm for 20, 25, 40% of 211, respectively.
- (2) 211 particles are effective crack blunters.
- (3) The morphology of 211 distribution depends on the start-up 211 particle size. 211 particles from precipitation having a tight size distribution give a more uniform 211 distribution in YBCO materials.
- (4) The twin spacing decreases with the interparticle spacing of 211 down to nanoscopic scale. Interpenetrating twins were observed in 40% and 50% percent 211 samples as well as in 30% sample that was doped with 0.5% Pt. Pt addition was found to be responsive for a even finer dispersion of 211 and therefore finer twin spacing results.
- (5) The critical current density was found to be the highest in the 40% 211 sample, which was 1×10^4 A/cm^2 at 77K in 1 Tesla.

94-32601



ABR

9

PUBLICATIONS

Microstructural Analysis of High Critical Current, Large Grained $\text{YBa}_2\text{Cu}_3\text{O}_{7-x}$ with Y_2BaCuO_5 Dispersion, Manoj Chopra, R. L. Meng, C. W. Chu, S. Jin, Siu-Wai Chan to be submitted to Physica C in September 1994. p.5-35 in this report.

Interface between Gold and Superconducting $\text{YBa}_2\text{Cu}_3\text{O}_{7-x}$, Siu-Wai Chan, Lie Zhao, Qi Li, D. B. Fenner, to be submitted to Applied Phys. Lett. September, 1994. p.61-81 in this report.

Use of Carbon Films for Passivation and Environmental Protection of $\text{YBa}_2\text{Cu}_3\text{O}_{7-x}$, Julie Dreyfuss Tatum, Siu-Wai Chan, Jack Tsai, Manoj Chopra, Julia Phillips, S. Y. Hou, to be submitted to Applied Superconductivity September, 1994. p. 36-60 in this report.

J. Appl. Phys. 72, 4220-4226 (1992)

The critical current density in High magnetic fields in epitaxial thin films of $\text{YBa}_2\text{Cu}_3\text{O}_{7-x}$: Flux pinning and pair-breaking. DP Hampshire and Siu-Wai Chan. p.82-89 in this report.

Appl. Phys. Lett. 63, 2964-2966 (1993)

Growth of Superconducting Y-Ba-Cu-O Films on Spinel and Garnet. Siu-Wai Chan, Manoj Chopra, Cheng-chung Chi, Tony Frey, Chang C. Tsuei. p. 90-91 in this report.

PROFESSIONAL PERSONNEL

Siu-Wai Chan Henry Krumb School of Mines,
School of Engineering and Applied Science,
Columbia University, New York, NY 10027
212-854-8519(tel),
212-854-8362(fax),
sc72@columbia.edu

Associate Professor of Materials Science and
Metallurgy

Julie Dreyfuss Tatum Graduated with a MS degree from Columbia U. in May 1994. She is now working at National Ceramic Company, Trenton, NJ.

**Lie Zhao,
Jack Tsai,
Manoj Chopra** Graduate Students in the same department

DTIC TAB	<input type="checkbox"/>
Unannounced	<input type="checkbox"/>
Justification	<input type="checkbox"/>
By	<input type="checkbox"/>
Distribution	<input type="checkbox"/>
Availability Codes	
Dist	Avail and/or Special
A-1	

Collaborating PROFESSIONAL PERSONNEL

DP Hampshire Lecturer at Durham University, UK

C.-C. Chi,

Tony Frey,

C. C. Tsuei

Researchers at IBM Yorktown Height, NY

Julia Phillips,

S. Y. Hou,

S. Jin

AT&T Bell Lab, Murray Hill, NJ

C. W. Chu

Ruling Meng

University of Houston, Texas.

D. B. Fenner

Li Qi

AFR, Inc., CT

INTERACTIONS (Coupling Activities)

CONTRIBUTED PRESENTATIONS:

- I. Nature of Grain Boundaries as Related to Critical Currents in $YBa_2Cu_3O_{7-x}$, at Nowick Symposium, Lehigh University, June 1994.
- II. Growth of Superconducting Y-Ba-Cu-O Films on Spinel and Garnet, M. Chopra, Siu-Wai Chan, C.C Chi, T. Frey, and C. C. Tsuei, at Materials Research Society Meeting December 1993.
- III. Microstructural Analysis of High Critical Current $YBa_2Cu_3O_{7-x}$ with 211 Dispersions, M. Chopra, S. Jin, R. Meng, C. W. Chu, S.-W. Chan, at Materials Research Society Meeting December 1993.

4

INVITED TALKS:

- I. Grain Boundaries and Critical Currents in Superconducting $\text{YBa}_2\text{Cu}_3\text{O}_{7-x}$, at University of Houston, TcSUH, TX, on April 22 1994.
- II. Degenerate Epitaxy, Coincidence Epitaxy and Origin of "Special Boundaries in Thin Films, at the Materials Science Society Annual Meeting, December 1993.
- III. Grain Boundaries and Critical Currents in Superconducting $\text{YBa}_2\text{Cu}_3\text{O}_{7-x}$, Gorgeia Institute of Technology, April 1994
- IV. Grain Boundaries and Critical Currents in Superconducting $\text{YBa}_2\text{Cu}_3\text{O}_{7-x}$, University of Washington, Seattle, May 1994.
- V. Conditions for Grain Boundary Wetting and the Subsequent Effect on Trans-boundary Critical Currents in $\text{YBa}_2\text{Cu}_3\text{O}_{7-x}$, at the Materials Research Society Meeting, San Francisco, April 14, 1993.
- VI. Nature of Grain boundaries as Related to Critical Currents in $\text{YBa}_2\text{Cu}_3\text{O}_{7-x}$, at the Workshop on Grain Boundaries in High Tc Superconductors, Univ. of Wisconsin-Madison, August 1992
- VII. Film Growth, Boundary Formation, and Critical Currents in $\text{YBa}_2\text{Cu}_3\text{O}_{7-x}$ at Argonne National Lab to their Materials Research group on superconductivity in September, 1992.
- VIII. Nature of Epitaxy, Grain Boundaries, Critical Currents in $\text{YBa}_2\text{Cu}_3\text{O}_{7-x}$ Thin Films, at International Superconductivity Technology Center (ISTEC), Tokyo, Japan, July 1992.
- IX. Grain Boundary Formation and Critical Currents in $\text{YBa}_2\text{Cu}_3\text{O}_{7-x}$ Thin Films, Industrial Technology Research Institute, Taiwan, July, 1992.
- X. Grain Boundary Formation and Critical Currents in $\text{YBa}_2\text{Cu}_3\text{O}_{7-x}$ Thin Films, National Tsing Hua University, Taiwan, July, 1992.
- XI. Grain Boundaries as related to Critical Currents in $\text{YBa}_2\text{Cu}_3\text{O}_{7-x}$, at the 94th Annual Meeting of the American Ceramic Society, Minneapolis, MN, April 1992.

None of the above trips for Chan's invited talks were paid from the AFOSR Grant.

MICROSTRUCTURAL ANALYSIS OF HIGH CRITICAL CURRENT, LARGE GRAINED $\text{YBa}_2\text{Cu}_3\text{O}_{7-\delta}$ WITH Y_2BaCuO_5

DISPERSSIONS.

Manoj Chopra, [†] R.L. Meng, [‡] C.W. Chu, [‡] S. Jin, ^{*} Siu-Wai Chan, [†]

[†]Henry Krumb School of Mines, Columbia University, N.Y. N.Y-10027

[‡]Texas center of Superconducting Research, Houston, T.X

^{*}AT&T Bell Labs, Murray Hill, N.J

A systematic microstructural study of large grained $\text{YBa}_2\text{Cu}_3\text{O}_{7-\delta}$ with various volume percentage of Y_2BaCuO_5 dispersions has been done. Microscopic and nanoscopic defect structures have been related quantitatively to the Y_2BaCuO_5 dispersions. The direct and indirect effects of the degree of Y_2BaCuO_5 dispersions have been discussed with respect to the overall microstructure and the critical currents (J_c).

I. INTRODUCTION

The process of Melt Texturing [1] holds great promise in improving the critical current densities (J_c) in $\text{YBa}_2\text{Cu}_3\text{O}_{7-\delta}$ (henceforth referred to as Y123 in this paper).

The increase of critical current density is achieved by an overall reduction in the content of high angle grain boundaries.[2] Previous studies have identified most of these high angle boundaries as "weak links".[3-4] Despite the reduction of these boundaries, the overall critical current (J_c) is not sufficiently high enough for commercial applications. The J_c of single crystal Y123 has been measured and has been found to be 10^4 Amps/cm². It is also essential that for large scale technological applications, that this material retain its high J_c in the presence of an external magnetic field. However, this goal has been eluding many researchers to date. Irradiation has proven to increase J_c for Y123,[2] though irradiation process is not likely to be economical. The effect of increasing J_c by Y_2BaCuO_5 (hence referred to as 211 in this paper) addition is discussed in this paper. Such additions have increased the J_c by a factor of 10 by inducing beneficial defect structures which enhance flux pinning.

The direct and indirect effects of 211 addition to Y123 is addressed quantitatively at both the microscopic and the nanoscopic levels. The effect of particle size and their relative distribution within the Y123 matrix is found to be of a considerable importance.

II. EXPERIMENTAL

A. Sample Preparation.

The melt textured samples are prepared by seeding the molten precursor with a single crystal $\text{SmBa}_2\text{Cu}_3\text{O}_{7-\delta}$ of size (0.25cm x 0.25cm)^[5], which has a higher peritectic temperature than that of Y123. This process promotes grain growth leading to large grain Y123. [2] Consequently, the large grain samples that we have examined have a grain size of 5 mm in thickness along the [001] direction of Y123 and is 20mm in diameter in the (001) plane. The Sm123 seed, has a cubic shape and facilitates the determination of the (001) and the (110) planes in the Y123 matrix during sectioning for subsequent microstructural analyses.

We have investigated both oxygenated and unoxygenated large grained Y123 samples having from 10% to 50 volume percent of 211 with a 10% increment in 211 volume% between samples. This variation in the starting 211 volume percentage is achieved by adding the corresponding amounts of 211 to the starting stoichiometric Y123 composition as the molten precursor.

B. Microstructural Analysis

A zoom in approach was adopted as the methodology for microstructural analysis. Defect structures such as cracks and the 211 dispersions are first observed using a Olympus Vanox AHMT optical microscope. While finer distributions of 211 dispersions along with extraneous phases and cracks were investigated with a S.E.M, J.E.O.L 35CF. Finally nanoscale structures, such as twins, dislocations, and stacking faults were examined under the transmission electron microscope (J.E.O.L 100CX).

Quantitative elemental compositions of different areas are evaluated using a calibrated electron microprobe (Cameca Camebax) while 211 size distributions are measured using the scanning electron microscope.

Samples for optical observations are prepared by grinding and polishing. This is done by lap polishing the samples using $0.5\mu\text{m}$ followed by $0.03\mu\text{m}$ alumina polish so as to obtain a mirror finish. Samples for S.E.M observation are prepared by depositing a thin layer of gold on the previously polished samples. Quantitative optical microscopy is performed on sections along the (001) and the (110) planes, with the assumption that the 211 distribution is isotropic in the (001) plane of Y123. Samples for Transmission Electron Microscopy (T.E.M) are prepared by mechanical polishing, dimpling followed by Argon ion-milling with liquid nitrogen cooling. Damage due to ion-milling is reduced by a final ion milling step at 3KV instead of 5KV [6]. The microstructure of Y123 in the orthorhombic state is analyzed quantitatively along (001) planar sections. Microstructural analysis is done before and after oxygenation of the large grained material. Different defect structures are then analyzed and related quantitatively in terms of the 211 volume percentage and the 211 interparticle spacing.

III. RESULTS AND DISCUSSION

A. Optical Microscopy

A typical optical micrograph of a 20% 211 dispersed in Y123 matrix is shown in (Fig.1). The variation of the final area fraction of the 211 particles with respect to the original volume percent of 211 particles is shown in Fig. 2. The area fraction (A_f) is defined as the ratio of the area occupied by the 211 particles as observed in the optical micrographs to the total sampled area in the (hkl) planar section[7] and can be expressed as

$$A_{\text{211}} = \frac{\text{Area occupied by 211}}{\text{Total sampled area}} \quad (1)$$

Our analysis (summarized in Fig.2) shows that the area fraction of the 211 particles increases with an increasing volume percentage of 211, for both (001) and (110) planar sections. In addition, the degree of anisotropy (τ) which is defined as the ratio of area fractions ($\tau = \frac{A_{\text{211}}^{(001)}}{A_{\text{211}}^{(110)}}$) of the 211 dispersions along the (001) and the (110) planes. This ratio peaks at 20% 211 with a value of 1.43 and decreases as the volume percentage of 211 increases further.

In pure single crystal Y123, the basal planes are known to grow at a faster rate in the lateral directions as compared to the other (hkl) planes.^[8] This relative difference in growth rates along different directions causes different growth retardation by the 211 particles, as the 211 addition increases from zero volume percent to 30 volume percent. Another consequence of the growth anisotropy is that with an increasing volume percentage of 211, the fast growing (001) plane encounters a greater number of 211 "barriers". Therefore, the degree of retardation is higher for directions contained in the basal plane as compared to those directions contained in the (110) plane. With an increasing volume percentage of 211 from 30% to 50%, the degree of anisotropy of 211 dispersion (τ) decreases to below unity. (Fig.2.)

The next part of the optical analysis involves studying the variation of the interparticle spacing ($\lambda^{(hkl)}$) with the volume percentage of 211. Ideally, the interparticle spacing is expressed below and defined as the mean free path or the average edge to edge distance between particles.^[7] :

$$\lambda^{(hkl)} = \frac{1 - A_f^{(hkl)}}{N_l} \quad (2)$$

where

$A_f^{(hkl)}$ is the area fraction of 211 in the (hkl) planar section, N_l is the number of 211 particles intercepted per unit length along lines drawn on sampled sections.

The number of 211 particles intercepted along a few test lines and the 211 area fraction are determined, the interparticle spacing $\lambda^{(hkl)}$ is then computed using equation (2). With an increasing volume percentage of 211, $\lambda^{(hkl)}$ decreases as shown in Fig.3. This reduction in $\lambda^{(hkl)}$ has an important effect on flux pinning and hence critical current (J_c). This will be discussed in section III.D.

Table III summarizes the analysis from optical microscopy on the 211 particles along the (001) and (110) planar sections in the large grained Y123. The calculated and the initially added 211 are compared (see Table III) and differences between the two values are noted (see columns D-A and D-G in table III). These differences can be attributed to liquid loss during melt processing. Such a loss in liquid during processing, leads to a net increase in the effective 211 volume percentage. Further there is an inherent under estimation of $A_f^{(hkl)}$, since any sub micron 211 particles which are beyond the optical resolution regime, are not considered in the calculation for $\lambda^{(hkl)}$.

B. Electron probe microanalysis (EPMA)

During the course of optical analysis, areas of relatively high reflectivity are encountered Fig.4. The compositions of these areas are determined using Electron Probe Microanalysis (EPMA) with calibrations based on standard samples of $\text{Cu}, \text{Y}_2\text{O}_3$ and BaSO_3 samples. Moreover E.P.M.A spectra were calibrated with the Y123 and the 211 areas on the melt textured samples. The size of the electron probe for the quantitative measurements is approximately $0.5\mu\text{m}$ which is smaller than the average size of the 211 particle. One of the typical areas sampled for E.P.M.A measurements is shown by an arrow in Fig. 5.

It is observed that the shining phase (region indicated in Fig.5 with a web like appearance) is predominantly copper rich. A comparison between the copper rich phase and Y123 is made and the results are shown in Table I. A similar comparison is also made with BaCuO_2 (Table II). The comparison shows the presence of a copper rich phase, (which is the frozen in liquid phase) implying that the peritectic reaction is usually incomplete when the overall volume percent of 211 is low ($\leq 20\%$ 211) or when the volume percent of 211 is low locally because of a non uniform distribution of 211 particles in the Y123 matrix.

C. Scanning Electron Microscopy (SEM)

The size and shape variation of the 211 particles is observed by using a JSM-35CF scanning electron microscope equipped with an Energy Dispersive Spectrometer (EDS). Various areas of the specimen are sampled and the 211 particle size is determined. It is observed that the 211 particle size is found to range from the sub micron to $23\mu\text{m}$ in diameter with a predominantly ellipsoidal shape of 211 particles as shown in Fig.6

D. Transmission electron Microscopy (TEM)

Finally, our study involves the observation of nanoscopic defect structures such as twins, dislocations and stacking faults using a T.E.M. The samples are mostly observed with a $[001]$ beam direction ($\vec{B} = [001]$). The goal was to observe :

- (i) The two twin variants and the variation in the twin spacing with 211 interparticle spacing.
- (ii) Dislocations and
- (iii) Stacking Faults

Previous studies have shown twin boundaries as centers of flux pinning, when the magnetic field is parallel to the twin plane [9-10]. Hence we observe the variation of the twin spacing and thus the twin density, with the 211 interparticle spacing.

Hence, a decrease in twin spacing and the correspondingly higher twin density would result in greater flux pinning by twin boundaries.

Similar analysis of twin spacing was performed for twinning in BaTiO₃.^[13] The variation of the twin spacing with varying grain sizes in Y123 is also reported^[12]. Here, we look at the variation of the twin spacing with increasing volume percentage of 211 as well as the local 211 particle spacing.

During the oxygenation (of Y123) and the subsequent transformation of tetragonal-to-orthorhombic (T→O), there are transformational shear strains which can be accommodated by the formation of twins along the (110) and (110) planes. Twin boundaries are manifestations of a counterbalance between the shear strain energy and the twin boundary energy. In the investigation involving the variation of twin spacing with grain size,^[12] elastic energy and total twin boundary energy was minimized by having the twin spacing follow the equation.

$$d = \sqrt{\frac{128\pi\gamma G}{ES^2}}^{[12]} \quad (3)$$

In their polycrystalline samples, neighbouring adjacent grains constrain the shape and the volume of the embedded, middle grain. Due to this shape/volume constraint, this embedded grain goes through the T→O transformation by internal twinning with a twin spacing that can be predicted by its initial size and shape following equation 3. For our present large grain samples, the constraint by adjacent grains is non-existent compared to the local constraints produced by the dispersed 211 particles. Thus with decreasing interparticle spacing, the strain energy per unit volume (w) increases in the constrained Y123 matrix. This increase in (w) manifests itself as fine twins which is shown in Fig.7.

Decreasing 211 interparticle spacing leads to an increasing transformational strain energy per unit volume (w) in the Y123 matrix, while the Y123 matrix is

constrained by the surrounding 211 particles. Such an increase in w causes finer twin spacing, formation of interpenetrating twins and a higher density of extended defects such as dislocations and stacking faults. Consequently, an increase in w also leads to higher magnitude of elastic stresses in the constrained Y123 matrix.

Hence in our present large grained samples, the high transformational strain energy can compensate for the increase in total twin boundary energy due to an increase in twin boundary area as a result of finer twins. The equilibrium twin spacing is determined by minimizing the sum of the total strain energy and the total energy of twin boundaries. Such a consideration in a first order results in the following formulation:[12]

$$T_w = \sqrt{\frac{K\gamma S_{211}}{E\epsilon^2}} \quad (4)$$

Where T_w is the twin Spacing, K is a geometric constant, γ is the twin boundary energy per unit twin boundary area, S_{211} is the local distance between two nearest Y123 / 211 interfaces in a direction perpendicular to the twin boundaries, E is the elastic modulus, ϵ is the strain associated with the $T \rightarrow O$ transformation along the (001) plane of Y123 {here $\epsilon = a/b-1$ }.

The above formulation does not take into account the elastic strain energy which is present at the 211/Y123 interface or the energy which goes into the formation of elastic serration's at the 211/Y123 interface. A plot between the twin spacing and the square root of the interparticle spacing, gives a linear fit. Such a plot is shown (for 40% 211, slope=2.3) in Fig.8. Similar plots on 20% and 30% 211 yield slopes of 2.4 and 2.2 respectively establishing the dependence of twin spacing with interparticle spacing rather than the volume percent of 211. From the slope of this curve the value of K is found to be ≈ 2570 m (as compared to $K= 402$ m[12]).

Another manifestation of the increasing strain energy per unit volume is the formation of interpenetrating twins. Interpenetrating twins have also been reported [12], though at a much larger scale (typical dimensions of such intersections as observed are nearly 40nm). Such areas represent regions of high strain energy and are energetically not favorable. However with increasing constraint (i.e. with decreasing interparticle spacing) such twins formations are found with increasing abundance as observed in a (001) planar sample ($\approx 40\%$ 211).

Such twin structures would be highly beneficial for flux-pinning because a fluxoid parallel to the twin plane, can be pinned more efficiently along both the twin directions in the twin plane. This is shown schematically in Fig.9. The efficiency of flux pinning in such a Y123 structure would be dependent on the size of the unit cell which is formed due to such twin intersections. Thus with a smaller cell size the flux line would be pinned better. Preliminary J_c measurements using the Bean's method show that the J_c is maximum for 40 volume percent 211 while it decreases with increasing volume percent 211 as shown in critical current measurements (Fig10). With decreasing Y123 superconducting volume, the decrease in J_c is not proportional to the volume decrease Fig.11. As observed from Fig.11 the normalized J_c for the 30% and the 40% 211 samples is relatively higher. This can be explained by the presence of increasingly efficient flux-pinning sites (such as the interpenetrating twins) which are formed with increasing volume percent of 211 starting between 30% to 40 volume percent of 211.

The 2% contraction along the [001] direction from the T \rightarrow O transformation is relieved partially by plastic deformation mechanisms dislocation motion in the basal plane as well as formation of stacking faults. Such dislocations and stacking faults have been seen in the Y123 matrix for cases when the 211 particles are in close proximity to each other, shown in Fig.12 and Fig.13

Another important observation made is that two twin variants were observed in a region between two 211 particles A and B (see Fig.14), where particle A being closer to a near by boundary, has two twin variants emerging from its interface with the Y123 matrix.

From this observation we postulate that the 211/Y123 is a short circuit pathway for oxygen diffusion since particle A is closer to the Y123 boundary which is known to provide a fast diffusion pathway for oxygen. Oxygen intercalation is necessary for the T \rightarrow O transformation. This short circuit pathway at the 211/Y123 interface leads to a higher oxygen concentration (i.e δ nearly equal to 0.1) at the 211/Y123 interface and therefore facilitates the T \rightarrow O transformation such that the propagation of the two twin variants are emerging from the 211/Y123 interface as shown in Fig.15.

IV. CONCLUSIONS

We have studied the multiple effects of 211 additions to Y123. Our results show that a increasing 211 volume percent in a Y123 matrix results in the formation of certain highly efficient flux pinning structures which has prevented an otherwise proportional reduction in J_c , despite a decrease in Y123 superconducting volume.

The addition of 211 has both a direct and an indirect effect on the J_c . The addition of 211 has indirectly affected microstructural features such as twin spacing and densities of dislocations and stacking faults. The variation of twin spacing has been systematically studied with samples containing different volume percentages of 211. We observed that the twin spacing decreases with increasing volume percent of 211 and more importantly within a finite volume percent of 211, the twin spacing decreases with the 211 interparticle spacing following equation 4. The 211/Y123 interface may act as a short circuit pathway for oxygen diffusion hence increase the rate and the extent of the T \rightarrow O transformation in a dense Y123 sample. This short circuit pathway of high oxygen concentration at the

Y123/211 interface also may enhance the formation of the two twin variants adjacent to each 211 particles.

V. REFERENCES

1. S.Jin, T.H. Tiefel, R.C.Sherwood, M.E.Davis, R.B.van Dover, G.W.Kammlott, R.A.Fastnacht and H.D. Keith : *Appl. phys.lett.* **52**, 2074, (1988)
2. M.Murakami, *Melt Processed High - Temperature Superconductors* (World Scientific. 1992) pp. 9,40,220,82
3. D.Dimos, P.Chaudhari and J.Mannhart : *Phys.Rev.B* **41**, 4038, (1990)
4. Siu-Wai.Chan, D.M.Hwang, R.Ramesh, S.M.Sampere, L.Nazar, R.Gerhardt and P.Pruna *AIP Conf.Proc.No.200* (AIP, New York, 1990) p.172.
5. R.L.Meng, Y.Y.Sun, P.H.Hor and C.W.Chu: *Physica C* **179** 149. (1991)
6. K.Kimura, M.Matsuo, M.Murakami, K.Sawano and S.Matsuda: *ISIJ International* **29** 213.(1989)
7. Vander Voort, *METALLOGRAPHY Principles and Practice* (Mc Graw-Hill Book Company 1984) pp 426, 480.
8. A.Goyal, K.B.Alexander, D.M.Kroeger, P.D.Funkenbusch, S.J.Burns : *Physica C* **210**, 197-212, (1993)
9. L.J.Swartzendruber, A.Roitburd, D.L.Kaiser, F.W.Gayle and L.H.Benett : *Phys.Rev.Lett* **64**, 483, (1990)
10. W.K.Kwok, U.Welp, G.W.Crabtree. K.G.Vandervoort, R.Hulscher and J.Z.Liu: *Phys.Rev.Lett* **64**, 966, (1990)
11. G.Arlt: *J. Mat.Sci* **25**, 2655-2666, (1990)
12. T.M.Shaw, S.L.Shinde, D.Dimos, R.F.Cook, P.R.Duncombe and C.Kroll : *J.Mater.Res* **4**, 248, (1989)
13. G.Arlt, D.Hennings and G.De With : *J.Appl.Phys.* **58**, 1619, (1985)

Figure Captions

Fig.1 Optical micrograph of 20 volume% 211 in an oxygenated Y123 matrix. Areas marked as A show 211 particles while B shows the presence of cracks parallel to the (001) plane of Y123.

Fig.2 Variation of 211 area fraction ($A_f^{(hkl)}$) with respect to volume percent 211.

Fig.3 Variation of 211 interparticle spacing with 211 volume percent along (001) and (110) planar sections.

Fig.4 Areas of high reflectivity as seen under the optical microscope. (Marked as A)

Fig.5 Secondary electron image of 20% 211 in Y123 matrix showing regions where EPMA is done (marked as A)

Fig.6 Back scattered electron micrographs of a 20% 211 in Y123 matrix showing shape and size dispersions of 211 particles.

Fig.7 Fine twins between 211 particles.

Fig.8 Variation of twin spacing with the square root of local 211 interparticle spacing for 40% 211 sample.

Fig.9 Schematic diagram of a fluxoid being trapped. The areas marked are possible regions of flux pinning.

Fig.10 J_c v/s H for various volume% of 211 in Y123 matrix.

Fig.11 Weighted J_c v/s Volume percent 211, showing evidence for increased efficiency of flux pinning with decreasing superconducting volume.

Fig.12 Presence of dislocations in the (001) basal plane of a 40% 211 sample

Fig.13 Presence of stacking faults and cracks in the vicinity of a 211 particle in the (001) basal plane of a 40% 211 sample. Viewed along a near [001] incidence.

Fig.14 Twins emerging from a 211/Y123 interface, with particle A closer to a boundary.

18

Table Captions

Tab.I Variation of liquid phase composition with respect to Y123 stoichiometry.

Tab II Variation of liquid phase composition with respect to BaCuO₂ stoichiometry.

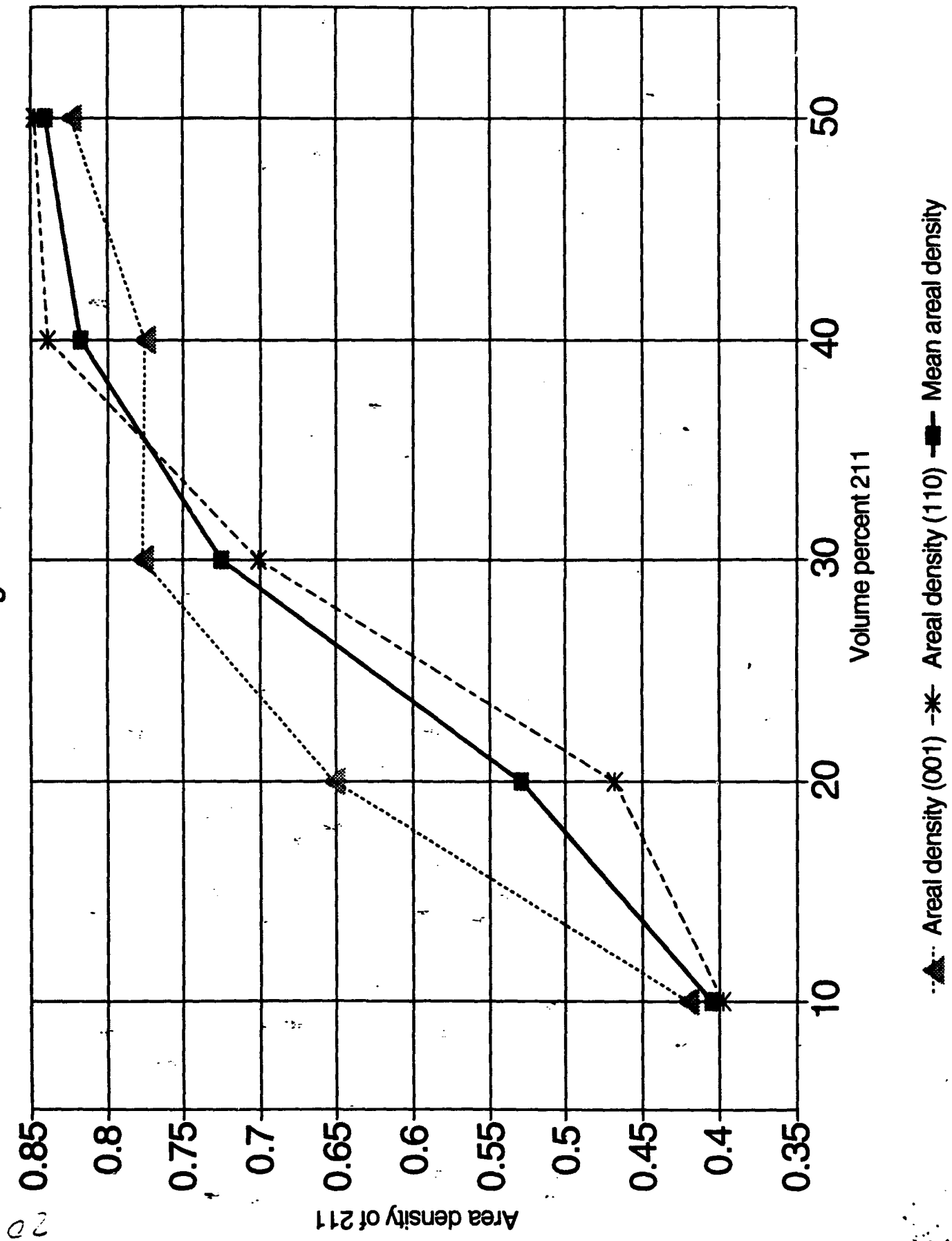
Tab.III Measurements done along (001) and {110} planar sections.



Fig. 1

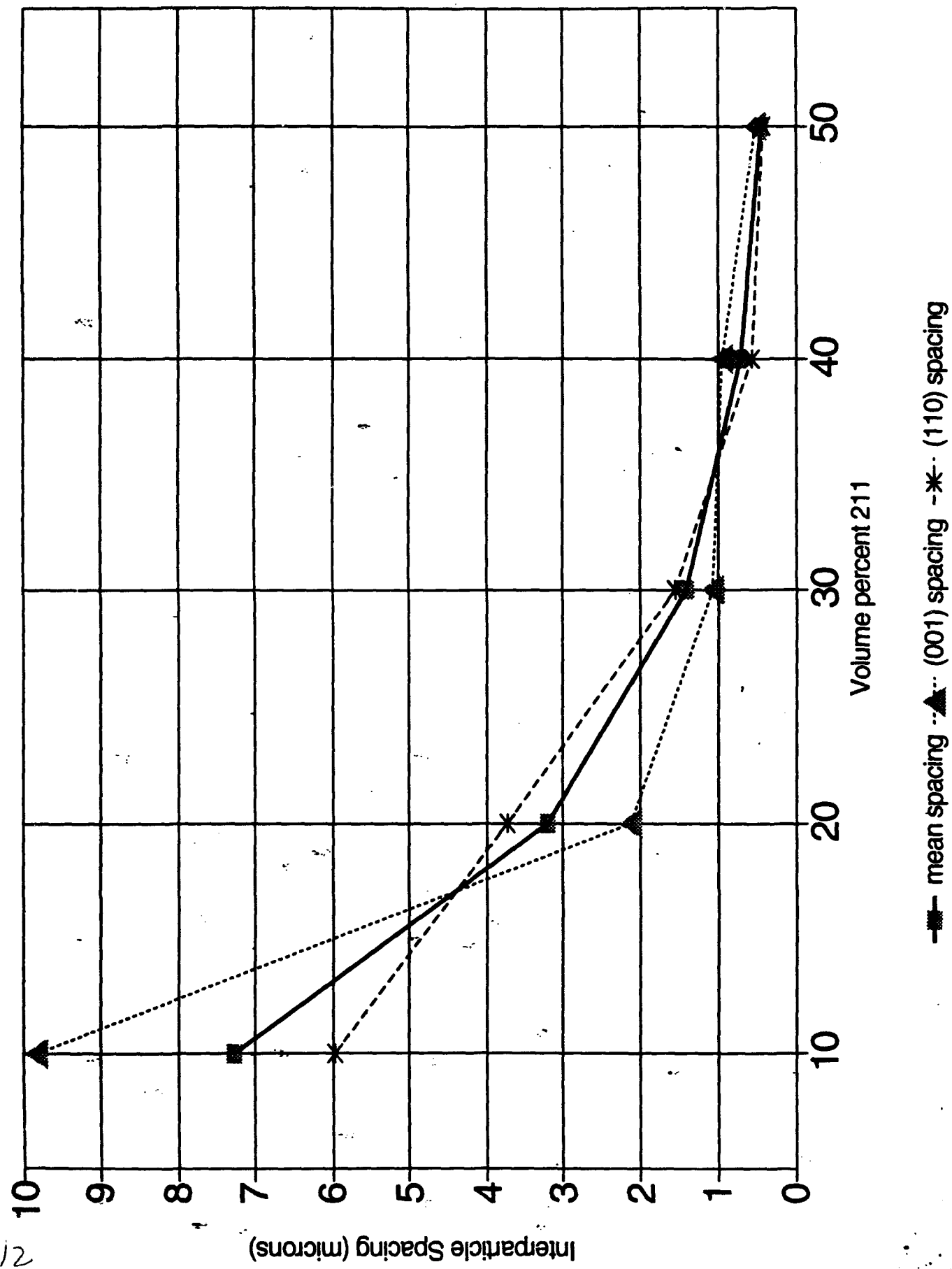
AREA DENSITY V/S 211 VOL %

Fig. 2



INTERPARTICLE SPACING V/S 211 VOL %

Fig.3



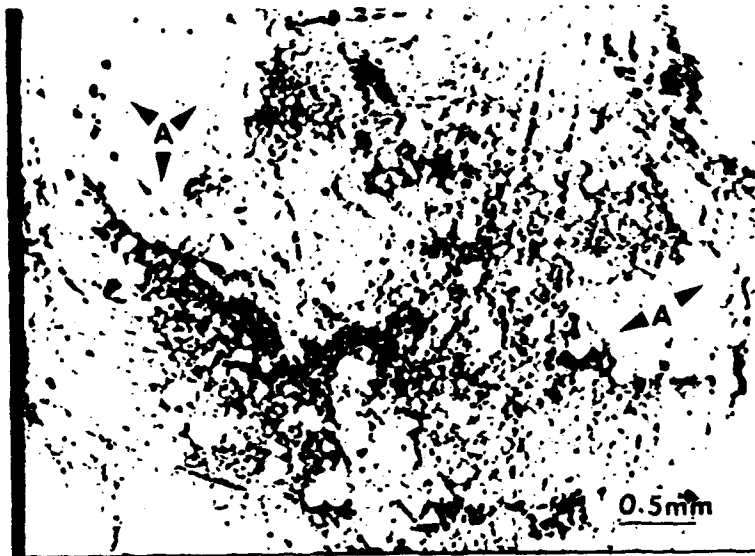


Fig.4

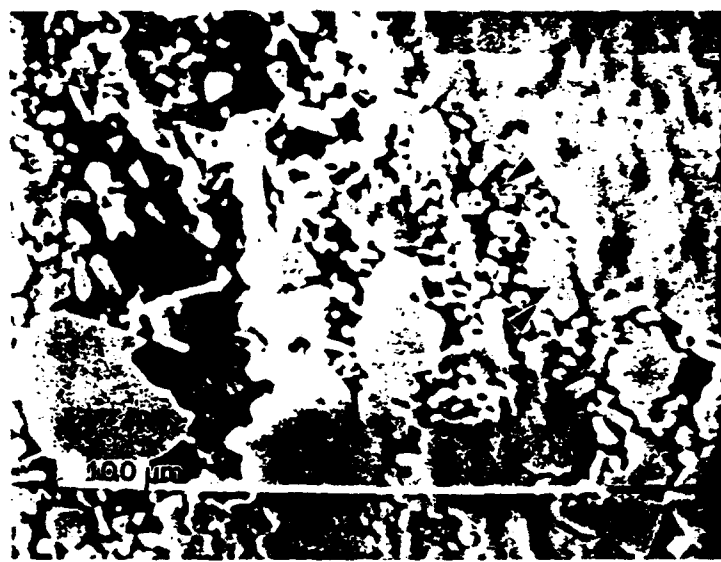


Fig.5

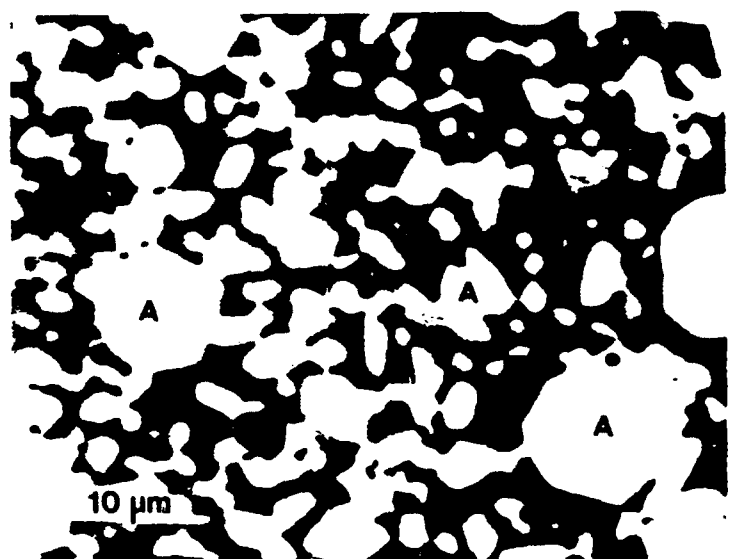
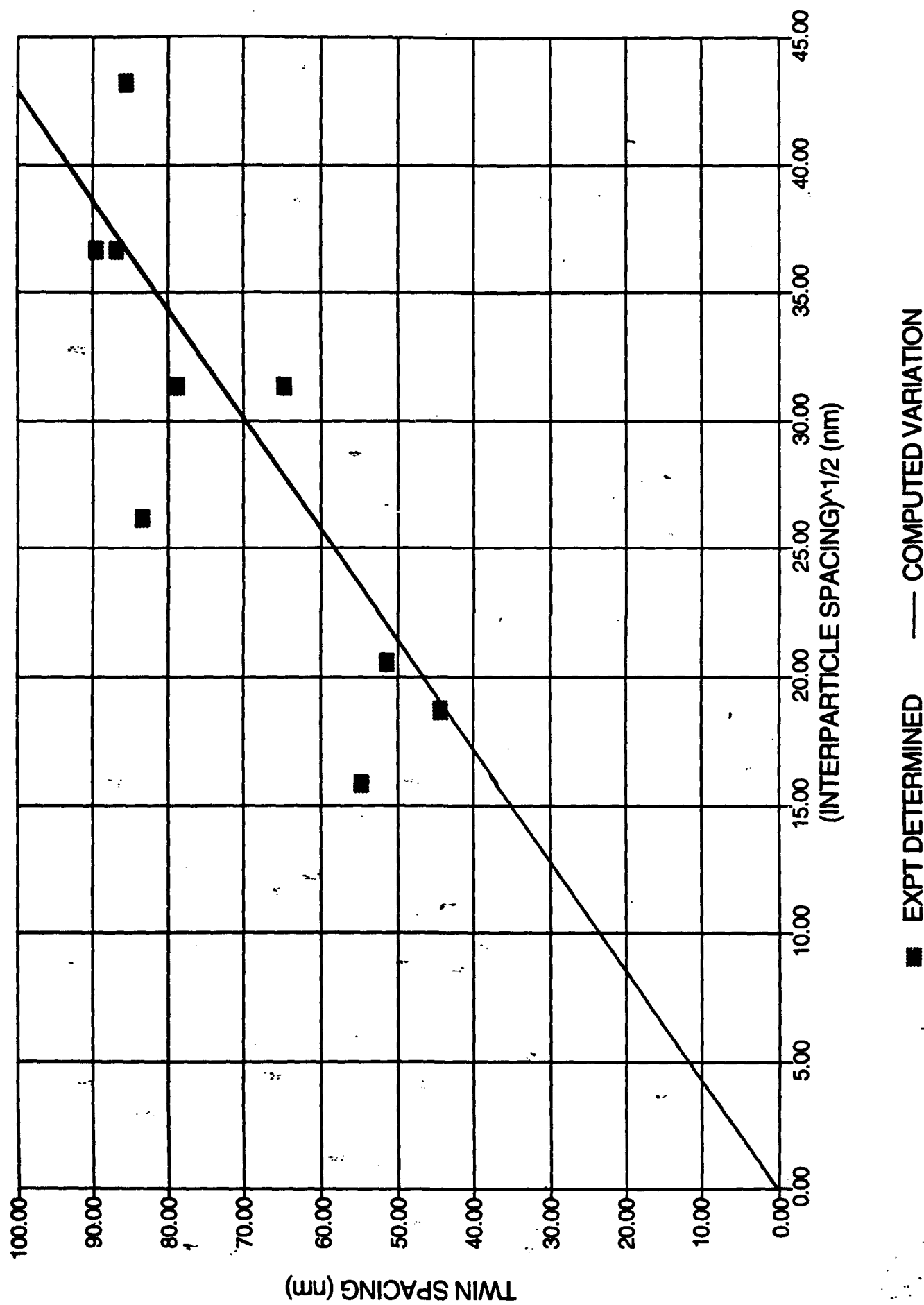


Fig.6



Fig.7

40% 211 ab OXY
Fig.8



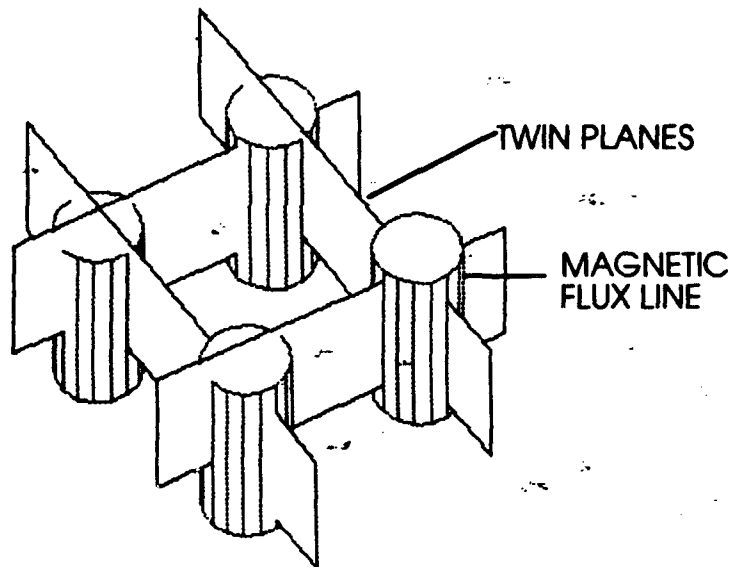
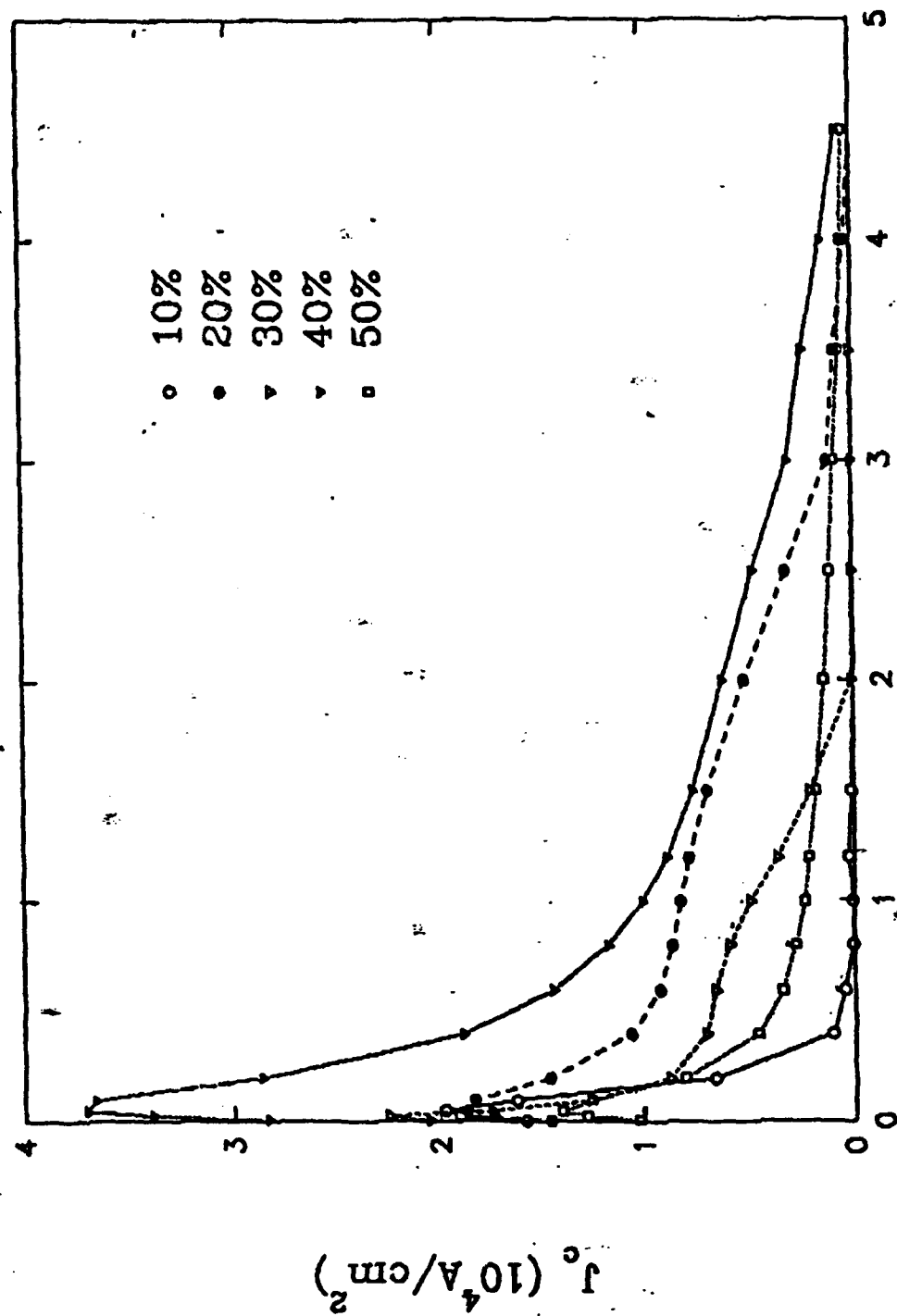


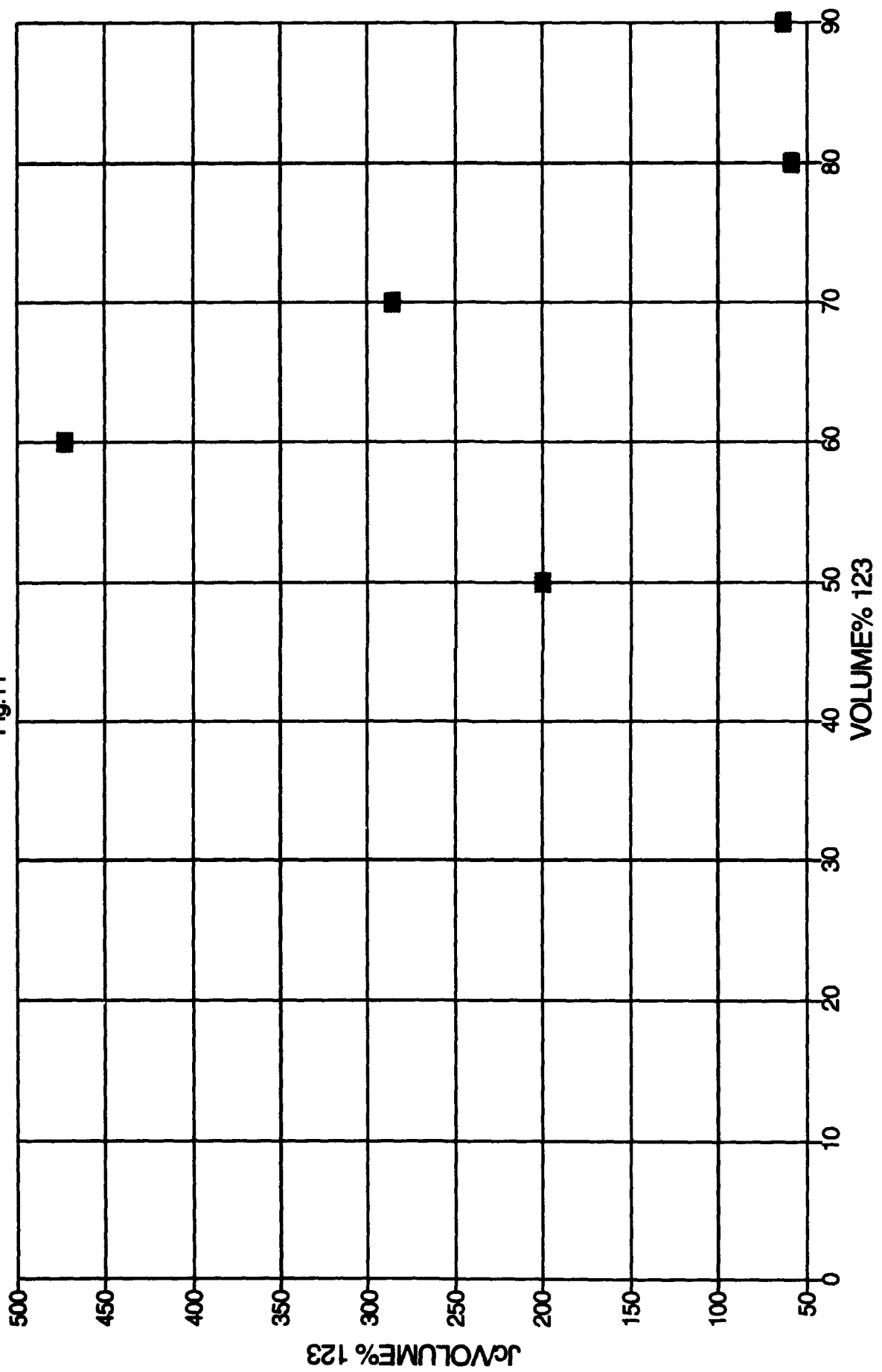
Fig.9

Fig.10



WEIGHTED J_c AS A FUNCTION
OF 123 VOLUME%

Fig.11



■ 123 VOLUME%

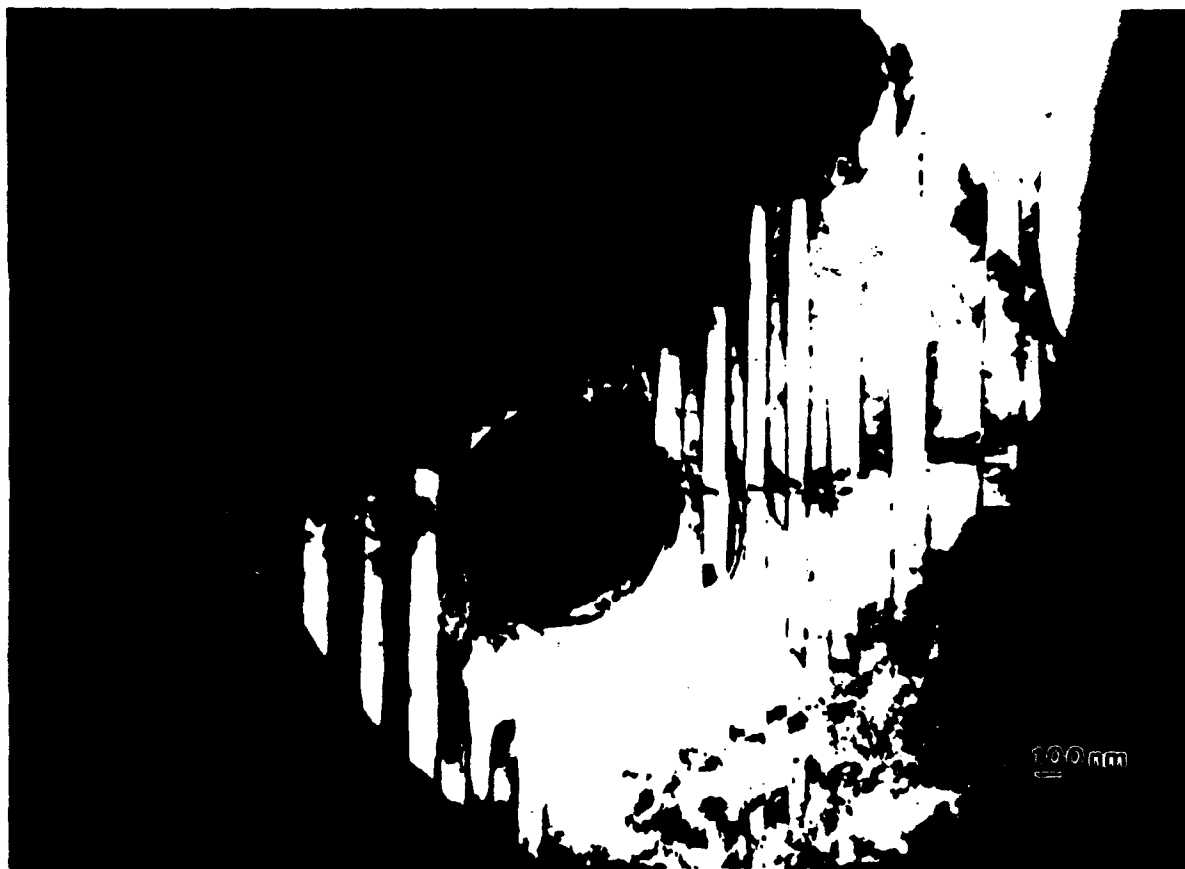


Fig.12

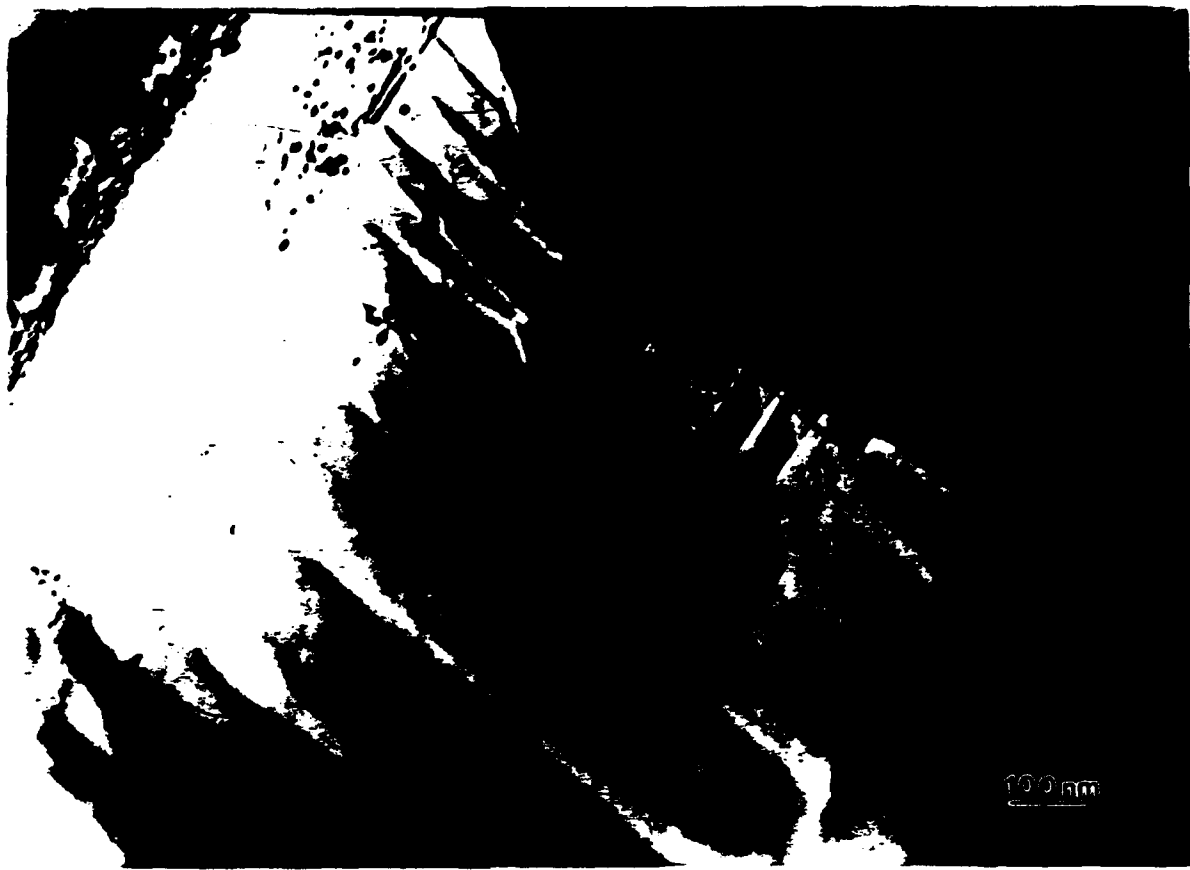


Fig.13



Fig.14

LIQUID PHASE COMPOSITION

AREA	YTTRIUM	BARIUM	COPPER
1.	0.44	0.31	8.06
2.	0.05	0.04	9.27
3.	0.57	0.27	8.26
4.	0.96	2.10	3.18
$\text{YBa}_2\text{Cu}_3\text{O}_{7-\delta}^*$	1.00	2.00	3.00

- The above table gives the elemental stoichiometry of the liquid phase with respect to $\text{YBa}_2\text{Cu}_3\text{O}_{7-\delta}$.
- * Thus area $\text{YBa}_2\text{Cu}_3\text{O}_{7-\delta}$ gives the elemental stoichiometry of $\text{YBa}_2\text{Cu}_3\text{O}_{7-\delta}$. This may be used as a standard for comparing the yttrium, barium and copper stoichiometries in the observed liquid phase.

Table.I

LIQUID PHASE COMPOSITION

AREA	BARIUM	COPPER
1	0.14	3.4
2	0.02	3.91
3	0.11	3.48
4	0.88	1.34
BaCuO_2^*	1.00	1.00

- The above table gives the elemental stoichiometry of the liquid phase when compared to BaCuO_2 (the predominantly liquid phase at the peritectic temperature).
 - * The figures corresponding to this area can be used to compare the other areas since they correspond to an exact BaCuO_2 stoichiometry.

Table.II

ACTUAL VOL % 211	AREA FRACTION OF 211 ALONG (110)	AREA FRACTION OF 211 ALONG (001)	MEAN AREA FRACTION (M)	CALCULATED VOL % 211	DIFFERENCE IN 211 VOLUME %	CALCULATED AREA FRACTION	DIFFERENCE IN AREA FRACTIONS	
							D = (C+2B)/3	D/3 x 100
A	B	C						
10	0.4203	0.397	0.4048	25.75	15.75	0.2154	0.1894	0.1894
20	0.6526	0.46809	0.5296	38.54	18.54	0.342	0.1876	0.1876
30	0.7759	0.70125	0.7261	61.87	31.87	0.4481	0.2778	0.2778
40	0.775	0.839	0.8177	73.94	33.94	0.5429	0.2748	0.2748
50	0.82413	0.8474	0.8396	82.413	32.413	0.623	0.2166	0.2166

TABLE III

Use of Carbon Films for Passivation and Environmental Protection of $\text{YBa}_2\text{Cu}_3\text{O}_{7-x}$

Julie Dreyfuss Tatum*, Siu-Wai Chan, Jack Tsai, Manoj Chopra
Columbia University

School of Engineering and Applied Science
Henry Krumb School of Mines
New York, NY 10027

Julia M. Phillips, S. Y. Hou
AT&T Bell Laboratories
Murray Hill, NJ 07974

(new)
*** Also at National Ceramic Company, Trenton, NJ 08602**

TABLE OF CONTENTS

Abstract	page 1
Introduction	page 1
Previous Experiments	page 4
Experimental Details	page 5
Results and Discussion	page 6
Conclusion	page 8
Acknowledgements	page 9

List of Tables

- I. Superconducting Data 4 hour, 22°C, 50% RH degradation
- II. Superconducting Data, 44.5 hour, 22°C, 100% RH degradation
- III. Transition Temperatures, 2 hour, 20°C, 100% RH degradation
- IV. Critical Current Density, 2 hour, 20°C, 100% RH degradation
- V. Room Temperature Resistivity, 2 hour, 20°C, 100% RH degradation

List of Figures

- 1. Optical micrograph showing 2 diamond-scribe marks defining a bridge of 53 x 53 microns**
- 2. Schematic Diagram of the T_c and J_c Measurement Apparatus**
- 3. Optical Micrograph showing crazing of DLC film after thermal shock of liquid nitrogen**
- 4. Schematic Diagram Showing the Set-up of the Degradation Apparatus for 100% RH**
- 5. Control - Transition Temperature**
- 6. Carbon - Transition Temperature**
- 7. Control - Critical Current Density**
- 8. Carbon - Critical Current Density**
- 9. SEM micrograph showing degradation of uncoated YBCO film**
- 10. SEM micrograph showing degradation of a-Carbon coated YBCO film**

ABSTRACT

Electronic device applications of high temperature superconductors require the production of patterned thin films which are stable and inert in various operating environments. However, the superconducting rare earth barium cuprates have been shown to decompose in water and to degrade in ~~under~~ superconducting properties ~~in~~ a humid atmosphere. Protective coatings or removable protective films can realize many applications and facilitate processing of superconducting devices. Here, diamond-like carbon films as well as amorphous carbon films are being investigated as possible protective layers for $\text{YBa}_2\text{Cu}_3\text{O}_{7-x}$ (YBCO). Amorphous carbon (a-carbon) films deposited by evaporation are shown to protect superconducting YBCO films from degradation by humidity. The YBCO films with a-carbon coating had critical current densities 4 orders of magnitude higher than the uncoated films after 2 hours at 100% RH stressing. The critical current is shown to be a better indicator for the degree of degradation, since the transition temperature remains relatively constant as long as there is enough YBCO phase to provide a percolation path for the supercurrent. Degradation was also evaluated by SEM micrographs.

INTRODUCTION

Several studies on the environmental degradation of the $\text{YBa}_2\text{Cu}_3\text{O}_{7-x}$ (YBCO) as well as interactions of YBCO with water and other solvents, showed that degradation processes were inevitable and irreversible¹⁻⁶. These results agree with the measured enthalpy (ΔH) of the detrimental reaction: $2 \text{YBa}_2\text{Cu}_3\text{O}_{7-x} (\text{s}) + 3 \text{H}_2\text{O} (\text{l}) \rightarrow 5 \text{CuO} (\text{s}) + 3 \text{Ba}(\text{OH})_2 (\text{s}) + \text{Y}_2\text{BaCuO}_5 (\text{s}) + (\frac{1}{2} - x) \text{O}_2 (\text{g})$ with a value of -496 kJ/mole at room temperature for $x = 0$.⁷⁻¹¹ The large negative value of enthalpy, which can be used to estimate free energy since the entropy contribution is small, indicates that the reaction is spontaneous. In particular, surface decomposition of YBCO in mild environments was observed by high resolution electron microscopy (HREM) and transmission electron microscopy (TEM).^{12,13}

There are some misconceptions that stoichiometric and highly [001]-oriented YBCO films are not susceptible to degradation. The degradation will be slower for such films, but it does occur, since it is a matter of kinetics and not thermodynamics. The surface decomposition, as observed by HREM,

occurs by insertion of an extra Cu-O layer along the (001) plane.¹² This process occurs less easily on a (001) surface, which explains the observation that c-oriented films are less susceptible to degradation. However, even highly c-oriented films do degrade. Besides, these films usually have a fair number of grains of other orientations. As-deposited films made by coevaporation of BaF₂, Y and Cu are robust because, unlike either Ba or BaO, BaF₂ is not hygroscopic.¹⁴ (See Appendix I). However, after annealing, these films consist of the YBCO phase and therefore, like other YBCO films, will be susceptible to degradation under ambient conditions. All YBCO films 1 μ m thick or thinner prepared by various methods (e.g. in-situ laser deposition, e-beam coevaporation) dissolve in 1 vol.% nitric acid in less than 30 sec.¹⁵ Processing of YBCO films requires methodical efforts to keep them dry.^{15,16} Even good YBCO films that give a high quality factor (Q) in microwave meander-line resonators can deteriorate in an unpredictable manner in spite of careful handling.¹⁷ Although more data exist on degradation of YBCO than on other superconducting rare earth barium cuprates, it is believed that, because of the similarity in valence and chemistry of yttrium and other rare earth elements, the other rare earth barium cuprates are also susceptible to degradation and can benefit from protective coatings similar to those used for YBCO. In YBCO, BaO is the most unstable of the constituent oxides, so any high temperature superconductor (HTSC) with BaO, or other alkaline earth oxides as a component, will presumably be subject to degradation in the presence of water vapor.

High T_c superconducting thin films, because of their low surface resistance, may find application in high frequency devices operating at microwave, radio, and mm-wave frequencies. Conductors used for high frequency devices need to have high surface conductivity. The surface conductivity of the superconducting materials at the operating temperature depends on the integrity of the surface layer to a thickness comparable with the magnetic penetration depth. The zero-temperature penetration depth λ_0 in YBCO thin films has been measured by various techniques to lie in the 150 - 300 nm range.¹⁷⁻¹⁹ The temperature dependence of the penetration depth in YBCO films follows the Gorter-Casimir relation $\lambda(T) = \lambda_0 / [1 - (T/T_c)^4]^{1/2}$.¹⁹ The measured effective penetration depth is known to increase with less than optimal YBCO films.¹⁹

Environmental degradation will reduce the surface connectivity of the superconducting

materials, reduce the critical current, reduce magnetic susceptibility, increase the surface resistance and therefore, degrade performance of devices that are made with HTSC materials. Hence, protective coatings for HTSC materials are important for device applications. Other coating methods that have been used include metals such as Ag or Au^{20,21}, and dielectrics such as MgO or LaAlO₃.²² These methods would be effective for building devices, but would be difficult to remove if used only as a temporary coating. Plasma polymerization of polymeric films has also been used to protectively coat YBCO. One polymer film had a composition similar to tetrafluoroethylene, but the YBCO reacted with the fluorine at the interface. The interfacial reaction would limit the commercial possibilities.²³ Polyacrylonitrile has also been used successfully as a water barrier. It is unclear whether there is any interfacial reaction, whether the film can be deposited directly in the YBCO film deposition chamber, or whether the polymer films can be easily removed for later YBCO film processing.²⁴

Carbon coatings of YBCO films have many advantages. Carbon does not react chemically with water, organic solvents, mild acids or bases. Therefore, a pinhole-free coating of carbon can provide a protective coating for YBCO or its hygroscopic precursors. The coating would be removed before annealing by oxygen plasma etching, and then reapplied to protect the YBCO before the next patterning step.

Carbon films, depending on the method of deposition, can exist at one extreme as amorphous/microcrystalline graphitic carbon films that are electrical conductors, or at the other extreme as "diamond-like" films that are insulating, scratch resistant, and transparent. The films can also exist in a continuum of polymeric states between the two extremes.²⁵ Some of the properties of these films depend on the methods as well as the conditions of deposition. In particular, "diamond-like" films with a dielectric constant around 5.5 can have a large range of measured dielectric loss. The loss depends on the species incorporated during deposition. Such a large variety of properties of the protective films can be highly desirable to tailor coating properties for each particular application for HTSC films.

The carbon films can be easily removed without residue by application of a room-temperature oxygen plasma. In addition, room-temperature plasma oxidation can enrich the oxygen content of

YBCO and improve superconducting properties.²⁶ Therefore, these carbon films can be used to protect the YBCO during harsh processing and later removed.

Deposition of these carbon films as well as their removal by oxygen plasma can easily be integrated into existing vacuum deposition chambers used for HTSC film deposition.²⁷ Such compatibility of different processes can lead to versatility in fabrication of device structures. For example, deposition of an in-situ carbon film right after the YBCO deposition can be used to protect YBCO films from degradation during transportation from one vacuum chamber to another. The pristine YBCO surface can be regenerated with the oxygen plasma in the second chamber before the next layer is deposited. This can be important for ex-situ layer-by-layer processing and complicated layering schemes for junction fabrication. Both carbon film deposition and removal by plasma oxidation can be accomplished with the YBCO films at room temperature.

PREVIOUS EXPERIMENTS

Previously, one of the authors (S.-W. Chan)²⁸ with L. Farrow had shown the deterioration of the characteristic YBCO Raman signal over the course of several hours of exposure in ambient air. In particular, the decreasing intensity and the down shift of the 500 cm⁻¹ mode has been related to the removal of oxygen in the YBCO films.²⁹ Encapsulation of these films with a 20 nm thick layer of "diamond-like" carbon film was accomplished by plasma polymerization of butane. The coatings were transparent to visible light, and the Raman spectra demonstrated that the YBCO films retained their good quality after the coating procedure and over the course of the day. Since it was found that a 200 nm diamond-like film will peel off due to its inherent compressive stress, the optimal thickness would appear to be between 20 nm to 200 nm.

Water permeability of both types of films was estimated by measuring the rate of perevaporation of water through a carbon-coated cellulose acetate film 25 microns thick. The DLC-coated cellulose acetate film was two times less permeable than the amorphous carbon-coated film, while the amorphous carbon-coated film was about four times less permeable to water vapor than the uncoated film.²⁸

EXPERIMENTAL DETAILS

YBCO precursor films 100 nm thick were deposited on LaAlO₃. Details of the coevaporation process are described elsewhere.³⁰ The precursor film was annealed to form the YBCO phase (see Appendix I). Samples were diamond scribed after annealing to form bridges for critical current measurements. A diamond scribe was attached to the z-axis of a micrometer stage, and the motion was controlled by the x- or y-axis micrometer. The diamond scribe was lowered onto the sample at one end, and then moved along to scratch the sample. Approximately halfway through the width of the sample, the diamond scribe was lifted, moved across the sample by approximately 100 microns, and then lowered again to complete the scratch. The discontinuity in the scratch formed the superconducting bridge for the critical current measurement. Bridges were measured using optical microscopy at 300X (see Figure 1). Widths of bridges were measured from the ends of the scratch, including any cracks, closest to the center of the bridge. Films of 20 nm Au and 100 nm Ag were evaporated onto the samples as contacting electrodes for conventional 4-point probe measurements. Masks were applied over the electrodes for samples that were to receive subsequent carbon coating.

Samples were divided into three groups: DLC coated, a-C coated, and control. An amorphous carbon film of 10 nm in thickness was evaporated in a Denton Vacuum Evaporator model 503FP at 10^{-5} torr using a graphite filament source as is typically done for scanning electron microscopy (SEM) of non-conductive samples. A 80 nm thick diamond-like carbon film was applied in a reactive ion etching (RIE) chamber first etching the samples for 10 seconds in oxygen at 40 mtorr and -350 volt bias, and then depositing DLC for 80 seconds using butadiene at 40 mtorr and -450 volt bias. The RIE chamber was manufactured by Oxford Plasma Technology.

All samples were measured for critical transition temperatures (T_c 's) and critical current densities (J_c 's) prior to any humidity stressing. Gold wires were bonded to the silver electrodes using indium as a solder. Samples were connected to the apparatus by mounting the 4 gold wires on brass screw contacts which connected to the voltage and current sources. Samples were cooled in liquid nitrogen, and then heated in ambient air to determine the superconducting transition temperature (T_c) using a current of 1 microamp. The measurement apparatus is shown in Figure 2. Critical current measurements were done immersed in liquid nitrogen (77 K). The current was manually increased from

one nanoamp in exponential increments (i.e. $\times 10$) until the voltage increased. Smaller increments were then used to get a smooth curve. The critical current was taken as an increase of one microvolt, which is twice the noise level of our equipment.

Four degradation conditions were used to evaluate the effectiveness of a-carbon as a protective coating for YBCO films. The first one was 4 hours in a closed chamber at 22°C with an ambient humidity of 50% RH. Samples were again stored in a dessicator until they were remeasured. No detectable degradation was seen (Table I). In subsequent experiments, to achieve 100% relative humidity, the air was bubbled through water, and then into the degradation chamber. The second condition was at 100°C, 100% RH for 30 minutes. This process completely destroyed the uncoated films, and degraded the coated samples to the point that the film was no longer continuous. New samples were prepared and degraded in a third condition at 22°C, 100% RH for 44.5 hours ($p_{H_2O} = 0.026$ atm, $p_{CO_2} = 0.0003$ atm). These samples were conducting, but no longer had a measurable critical current. New samples were again prepared, and degraded in a fourth condition for 2 hours at 20°C, 100% RH ($p_{H_2O} = 0.023$ atm, $p_{CO_2} = 0.0003$ atm). The degradation apparatus is shown in

Figure 3.

RESULTS AND DISCUSSION

The DLC coated samples had two processing problems: the large compressive stress in the DLC film caused existing cracks near the bridge to propagate, which made the bridge narrower in one case, and caused an open circuit in another. In addition, the DLC film delaminated during the measurement from the thermal shock of the liquid nitrogen and due to a large difference in thermal expansion coefficients (see Figure 4), and began to peel off after repeated measurements. Therefore, DLC films have potential to be used as an effective coating between processes that would not be subject to thermal shock, or if deposition procedures were developed to deposit films with a lower compressive stress.

The critical transition temperature (T_c) was taken as the midpoint of the transition. The transition width was measured as between 10% of the transition from the superconducting baseline, and 90% to the resistive state.

The data for samples degraded for 4 hours at ambient humidity are shown in Table I. No significant difference between coatings is noted. The data for samples degraded for 44.5 hours at 22°C and 100% relative humidity (RH) are shown in Table II. Measurements of T_c and J_c could not be made after this degradation process since the critical currents of the samples were lower than the lowest setting of the current source (1 nanoamp).

Perhaps, the fourth condition which is 2 hours at 20°C, 100% RH, gives the most important comparison of T_c and J_c . The T_c and transition width data before and after degradation are shown in Table III. The T_c on samples before degradation ranged from 87 to 91K, and after degradation was between 86 and 90K. The transition widths before and after degradation show a clear difference between sample groups. The average transition width for the a-C samples before degradation is 1 degree, and after degradation is 4.7 degrees. For the control samples, the average transition width before degradation is 2.7 degrees, and after degradation is 9.3 degrees (see Figures 5 and 6). The offset in Figure 5 is due to the severity of the degradation.

The J_c measurements show the most dramatic difference between sample groups (see Table IV and Figures 7 and 8). The critical current density for all samples before degradation was on the order of 10^5 amps/cm² or greater. The a-C coated samples had a critical current density higher than could be measured by the current source ($> 10^6$ amps/cm²). The values however are close to the maximum J_c of 10^7 amps/cm² at 77K that has been observed for YBCO thin films. The J_c measurements after degradation for a-C coated samples are between 10^4 and 10^6 amps/cm². They all decreased from the initial measurements, and none exceeded the measurement capability of the current source as happened before degradation. There was some degradation of the superconducting films, but the critical current densities are still high enough for use in electronic devices. The control samples had decreased in critical current density to the point that they would be no longer useable as superconductors in devices. The J_c measurements ranged from 0.1 to 1.75 amps/cm².

The room temperature resistivities (see Table V) increased slightly in both the control and a-C sample groups after degradation. There is not enough of a change to differentiate sample groups, although all samples have obviously shown some degradation over the two-hour period due to the

consistent higher resistivity after degradation.

Scanning electron microscopy (SEM) was applied to examine the degraded film surfaces. SEM analysis of the degraded films shows that more features are apparent on the control sample (see Figures 9 and 10). The original, undegraded films are all smooth and featureless. The degradation begins as small pits which expand to cover a larger area as the degradation progresses resembling a nucleation and growth process. Comparison of the micrographs of the coated and uncoated samples reveals that the degraded areas are larger by a factor of 100 in the control sample than the a-C coated sample. The mode of degradation appears to be similar in both samples.

The a-C film is effective for preventing degradation by the effects of water vapor for short periods of time (2 hours), at ambient conditions (see Table I). Further study will be needed to determine the threshold at which the coating is no longer effective to maintain useable superconducting properties of the YBCO. By coating the YBCO, the degradation is significantly decreased as demonstrated by the SEM micrographs and the critical current densities. The a-C coating is not completely effective as a passivation layer since it does not form conformal coatings and is not totally impermeable to water, and some degradation was observed even in coated samples. Since the YBCO films are c-axis oriented, some of the degradation may have occurred due to penetration of the water vapor underneath the carbon film, at the a-C/YBCO interface.

CONCLUSION

The a-C coating is effective as a passivation layer for short-term storage of YBCO thin films in ambient conditions during device processing. At longer times (greater than 1 day) at high relative humidity levels ($p_{H_2O} = 0.026$ atm) and ambient temperature, significant degradation occurs, and both coated and uncoated samples are observed to degrade to different extents. Since water vapor is the critical reactant, degradation for 2 hours at 100% RH degraded the samples more than degradation for 4 hours at ambient humidity, which produced no significant change in J_c . The critical current density is the most significant parameter to indicate the level of degradation. In this case, the a-C coated YBCO films had critical current densities 4 orders of magnitude higher than the uncoated films after stressing 2 hours at 100% RH. The a-carbon coating can be used to minimize short term degradation for YBCO

superconductors in humid conditions, although the degradation will proceed at a much slower pace.

ACKNOWLEDGEMENTS

J.D.T. would like to thank Ms. Martha Yarufinski and Ms. Dee Lewis Breger for their assistance in carbon deposition, Dr. Antoni S. Gozdz for a-C:H (DLC) deposition, Mr. George Leou for assistance in building the diamond scribing and T_c and J_c measurement apparatus, and Mr. Julio Rodriguez for assistance with measurements. S.-W.C. would like to acknowledge the support from the National Science Foundation under grant #DMR-93-50464. M.C. acknowledges the support from the Air Force Office of Scientific Research, under grant AFOSR F49620-92-J-0160.

Table I

Superconducting Data before and after first condition: 4 hour, 22°C, 50% RH degradation

<u>Sample</u>	<u>BEFORE</u>		<u>AFTER</u>	
	<u>T_c(K)</u>	<u>Transition Width</u>	<u>T_c(K)</u>	<u>Transition Width</u>
<u>α-Carbon</u>				
2	90	1	89	1
1	88	1	88	1
10	89	1	89	1
<u>Control</u>				
4	88	5	88	5
11	91	1	86	2
16	90	3	89	3

Table II

Superconducting Data for the third condition: 44.5 hour, 22°C, 100% RH degradation

Sample	T_c (K)	Transition_Width (K)	J_c (amps/cm ²)	BEFORE	BEFORE	BEFORE	BEFORE	BEFORE	BEFORE
				Room Temperature	Room Temperature	Room Temperature	Room Temperature	Room Temperature	Room Temperature
Control									
E	89	1	7.78×10^5	3.20×10^7	6.95×10^3				
G	89	1	9.52×10^5	1.10×10^6	-a				
H	89	1	1.63×10^5	1.75×10^6	5.3×10^4				
J	89	1	5.00×10^6	3.70×10^7	-a				
K	88	1	2.78×10^6	1.50×10^6	5.98×10^4				
AVERAGE				1.43×10^6	5.04×10^6	3.99×10^4			
a-C									
B	86	2	1.67×10^4	1.00×10^6	1.71×10^2				
C	89	1	1.67×10^6	6.00×10^8	5.80×10^0				
D	88	2	4.17×10^4	2.20×10^7	5.57×10^1				
F	84	3	2.38×10^5	2.10×10^7	1.16×10^2				
I	87	1	1.11×10^6	1.70×10^7	1.78×10^2				
L	88	1	8.33×10^4	9.00×10^8	8.40×10^1				
N	88	5	1.19×10^5	1.80×10^7	4.23×10^2				
AVERAGE				4.53×10^5	2.76×10^7	1.48×10^2			

-a - too large to be measured

Table III

Transition Temperatures for the fourth condition: 2 hour, 20°C, 100% RH degradation

Sample	BEFORE		AFTER	
	T_c (K)	Transition Width	T_c (K)	Transition Width
a-Carbon				
3	91	1	88	2
4	91	1	88	6
8	89	1	86	6
Control				
2	90	1	87	8
5	87	2	89	10
7	89	5	90	10

Table IV

Critical Current Density for the fourth condition: 2 hour, 20°C, 100% RH degradation

<u>Sample</u>	<u>BEFORE</u>	<u>AFTER</u>
	J_c (Amps/cm ²)	J_c (Amps/cm ²)
a-Carbon		
3	$> 1.28 \times 10^6$	1.03×10^6
4	$> 1.52 \times 10^6$	4.55×10^5
8	$> 9.52 \times 10^5$	4.76×10^4
Control		
2	4.00×10^5	1.33×10^0
5	1.05×10^5	1.75×10^0
7	1.08×10^5	1.08×10^{-1}

Note: The critical current density measurements on the a-Carbon samples all exceeded the capacity of the meter so the actual values are higher, but would not be expected to be higher than 10^7 , since that is the highest critical current density observed for YBCO films of this type.

Table V

Room Temperature Resistivity for the fourth condition: 2 hour, 20°C, 100% RH degradation

<u>Sample</u>	<u>BEFORE</u>	<u>AFTER</u>
	ρ (Ohm-cm)	ρ (Ohm-cm)
a-Carbon		
3	6.54×10^{-5}	7.37×10^{-5}
4	4.47×10^{-5}	7.19×10^{-5}
8	3.42×10^{-5}	3.70×10^{-5}
Control		
2	1.61×10^{-5}	2.07×10^{-5}
5	1.06×10^{-4}	1.80×10^{-4}
7	8.76×10^{-5}	1.40×10^{-4}



Figure 1

Optical micrograph showing 2 diamond-scribe marks defining a bridge of
53 microns wide and 53 microns long.



Figure 4

**Optical Micrograph showing the crazing of a DLC film on YBCO film
after the thermal shock of liquid nitrogen**

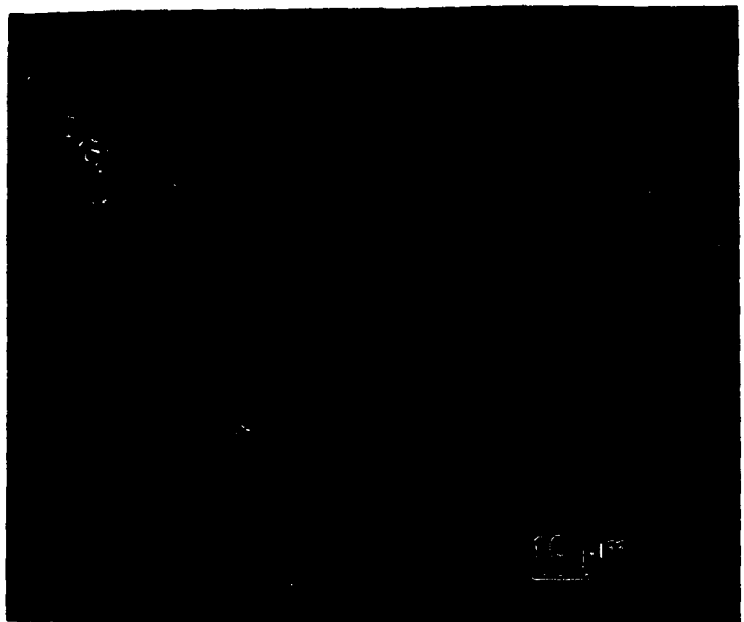


Figure 9

SEM micrograph showing degradation of uncoated YBCO film

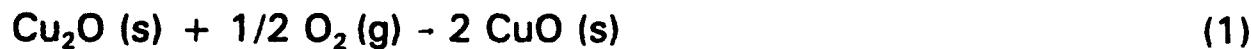


Figure 10
SEM micrograph showing degradation of a-Carbon coated YBCO film

Appendix I

Thermodynamics of Barium Fluoride Precursor Method

3 simultaneous reactions during annealing of precursor films of Y-Ba-Cu-F-O in H₂O and O₂:



$$\Delta H = 2(-157.3) - (-168.6) = -146 \text{ kJ/mol} \quad \text{--(ref. 11)}$$

$$\Delta S = 2(42.63) + 0.5(205.14) - (93.14) = 94.69 \text{ J/mol-K} \quad \text{--(ref. 11)}$$

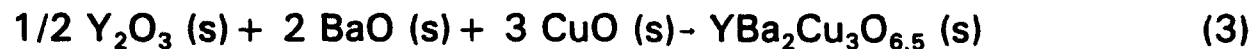
$$\Delta G = -146 - (.0947)(T) + 0.5(.008314)(T)\ln(p\text{O}_2) \text{ kJ/mol}$$



$$\Delta H = -553.5 + 2(271.1) - (-1207.1 - 285.83) = 397.23 \text{ kJ/mol} \quad \text{--(ref. 11)}$$

$$\Delta S = 70.42 + 2(173.8) - (96.36 + 69.91) = 251.71 \text{ J/mol-K} \quad \text{--(ref. 11)}$$

$$\Delta G = 397 - (0.251)T - .008314(T)\ln(p^2\text{HF}/p\text{H}_2\text{O}) \text{ kJ/mol}$$



$$\Delta H = -80.1 \text{ kJ/mol} \quad \text{-- ref. 10 (calorimetry)}$$

$$\Delta H = -21.4 \text{ kJ/mol} \quad \text{-- ref. 8 (emf)}$$

$$\Delta H = -109 \text{ kJ/mol} \quad \text{-- ref. 9 (emf)}$$

$$\Delta S = 29 \text{ J/mol-K} \quad \text{-- ref. 8 (emf)}$$

$$\Delta S = -4.6 \text{ J/mol-K} \quad \text{-- ref. 9 (emf)}$$

$$\Delta G = -109 + 4.6 \times 10^{-3} (T) \text{ kJ/mol} \quad \text{-- ref. 9 (emf)}$$

$$\Delta G = -80.1 - 0.029 (T) \text{ kJ/mol} \quad \text{-- } \Delta H \text{ from ref. 10, } \Delta S \text{ from ref. 8}$$

$$\Delta G = -21.4 - 0.029 (T) \text{ kJ/mol} \quad \text{-- data from ref. 8 (emf)}$$

The above values of Gibbs Free Energy can be used to calculate the temperature and oxygen partial pressure that will be thermodynamically favorable for the annealing process.

References

1. Fitch, L.D. and Burdick, V.L., J. Am. Ceram. Soc., **72**, (10), 1989, pp. 2020-2023.
2. Yan, M.F., Ling, H.C., OBryan, H.M., Gallagher, P.K., and Rhodes, W.W., Materials Science and Engineering, **B1**, 1988, pp. 119-129
3. Yokota, K., Kura, T., Ochi, M., and Katayama, S., Japan J. Appl. Phys., **29**, (7), 1990, pp. L1425-L1427
4. Barns, R.L., and Laudise, R.A., Appl. Phys. Lett., **51**, (17), 1987, pp. 1373-1375.
5. Bansal, P., and Sandkuhl, A.L., Appl. Phys. Lett., **52**, (4), 1988, pp. 323-325.
6. Garland, M.M., J. Mater. Res., **3**, (5), 1988, pp. 830-831.
7. Naito, N., Kafalas, J., Jachim, L., and Downey, M., J. Appl. Phys., **67**, (7), 1990, pp. 3521-3523
8. Idemoto, Y., Takahashi, J., and Fueki, K., Physica C, **194**, 1992, pp. 177-186.
9. Fan, Z., Ji, C., Zhao, Z., Journal of Less Common Metals, **161**, (49) 1990, pp. 49-59.
10. Zhou, A., Navrotsky, A., J. Mater. Res., **7**, (11), 1992, pp. 2920-2935.
11. Lide, David, ed., The NBS Tables of Chemical Thermodynamic Properties, National Bureau of Standards, 1982.
12. Wada, O., Odaka, T., Wakata, M., Ogama, T., and Yosidome, A., J. Appl. Phys., **68**, (10), 1990, pp. 5283-5288.
13. Pham, D.K., Zhao, R.P., Fielding, P.E., Myhra, S., and Turner, P.S., J. Mater. Res., **6**, (6), 1991, pp. 1148-1155.
14. Mankiewich, P.M., Scofield, J.H., Skocpol, W.J., Dayem, A.H., Good, E., Appl. Phys. Lett., **51**, 1987, p. 1753.
15. Private communication with T. L. Cheeks, Bellcore, Red Bank, NJ.
16. Private communication with V. Pendrick, David Sarnoff Research Center, Princeton, NJ.
17. Hylton, T.L., Beasley, M.R., Kapitunik, A., Carini, J.P., Darbeck, L., and Gruner, G., IEEE Trans. Magn., **Mag-25**, 1989, p. 810.
18. Fiory, A.T., Hebard, A.F., Mankiewich, P.M., and Howard, R.E., Phys. Rev. Lett., **61**, 1988, p. 1419.
19. Anlage, S.M., Sze, H., Snortland, H.J., Tahara, S., Langley, B., Ecom, C.B., and Beasley, M.R., Appl. Phys. Lett., **B51**, 1987, p. 622.
20. Ma, Q. Y., Schmidt, M.T., Weinman, L.S., Yang, E.S., Sampere, S.M., Chan, S.W., J. Vac. Sci. Technol., **A9**, (3) 1991, pp. 390-393.
21. Mogro-Campero, A., Turner, L.G., "The effect of Ag or Au overlayers on underlying $YBa_2Cu_3O_x$ thin films", to be published, 1994.

References, cont'd

22. Mallory, D.S., Kadin, A.M., and Ballentine, P.H., SPIE, Superconductivity Applications for Infrared and Microwave Devices II, 1991, pp. 66-76
23. Morohashi, S., Tamura, H., Yoshida, A., and Hasuo, S., Materials Science and Engineering, A109, 1989, p. 321-323.
24. Kale, S., Swaminathan, M., Ogale, S.B., Thin Solid Films, 206, 1991, pp. 161-164.
25. Mort, J. and Jansen, F., Plasma Deposited Thin Films, CRC Press, Inc. 1980, pp. 89-127.
26. Bagley, B.G., Greene, L.H., Tarascon, J.M., and Hull, G.W., Appl. Phys. Lett., B51, 1987, p. 622.
27. Sun, J.Z., Gallagher, W.J., Callegari, A.C., Foglietti, V., and Koch, R.H., Appl. Phys. Lett., 63, 1993, p. 1561.
28. U.S. Patent #5,087,608. February 11, 1992, "Environmental Protection and Patterning of Superconducting Perovskites, S.W. Chan and L.A. Farrow.
29. Chan, S.W., Greene, L.H., Feldmann, W.L., Miceli, P.F., and Bagley, B.G., AIP Conference Proceedings: Thin Film Processing and Characterization of High Temperature Superconductors, (165), 1988, p. 28.
30. Siegal, M.P., Phillips, J.M., Hsieh, Y.F., and Marshall, J.H., Physica C, 172, 1990, p. 282.

Interface between Gold and Superconducting $YBa_2Cu_3O_{7-x}$ (YBCO).

Siu-Wai Chan, Lie Zhao

**Department of Chemical Engineering,
Materials Science and Mining Engineering,
Henry Krumb School of Mines,
Columbia University,
New York, New York 10027**

Qi Li, D. B. Fenner

**A F R, Inc.
East Hartford, CT 06108**

ABSTRACT

Gold and silver are known to be important contact metals on $\text{YBa}_2\text{Cu}_3\text{O}_{7-x}$ (YBCO). Both metals have been used as additives in fabricating tapes of YBCO and $\text{Bi}_2\text{Sr}_2\text{CaCu}_2\text{O}_8$ (BSCCO) materials and have favorable results in improving not only the flexibility but also the weighted critical currents of the resulting composites. Previous results on S/N/S and S/N/S' junctions made using YBCO/Au/YBCO and YBCO/Au/Nb demonstrated that a supercurrent can be induced in the normal metal layers through the proximity effect. Our transmission electron microscopy of the Au/YBCO interfaces shows well-bonded interface with no extraneous phases present. Lattice fringes of the (001) plane in YBCO terminated at the interface abruptly. This observation support previous results of contact resistance and X-ray photoelectron spectroscopy (XPS). Both (001) integral steps and multiples of $1/3(001)$ steps were observed at the Au/YBCO interface. When the top gold layer was absent locally, surface degradation was observed as the (001) lattice fringes stopped short from the surface by 10 nm. Our results support that Au is a desirable contact metal and a dependable surface passivation material for YBCO.

INTRODUCTION

For the $\text{YBa}_2\text{Cu}_3\text{O}_{7-x}$ (henceforth referred to as 123 or YBCO) materials to be useful as supercurrent conductor for electromagnet, YBCO materials need to be fabricated into flexible tapes or wires

with high flux pinning capabilities. Unlike other reactive metals (e.g. Cu, Ti, Nb and Sn) which strongly react with oxygen and can form an insulating oxide layer at the interface as well as a non-superconducting layer on the YBCO surface due to depletion of oxygen¹, noble metals like silver and gold are phase compatible with YBCO and have been used as additives to increase flexibility in the resulting superconducting composites. Moreover, shank materials, i.e. normal metals are needed to carry overflow current and conduct away heat when a small part of the YBCO materials goes normal. Transport across YBCO/metal interface is important for the use of the normal metals as a shank as well as for S/N/S junction devices which use two such interfaces. The understanding of these technologically important interfaces is essential in order to harness YBCO for electrical power applications as well as for S/N/S junction devices.

Various research groups have been successful in improving critical current J_c by processing High Temperature Superconducting Cuprates (HTSC) with silver. Critical currents greater than 10^4 A/cm² at 4.2 K and 10-26 T in silver-sheathed BSCCO wire were prepared by Heine et. al. of Vacuumschmelze². Osamura et.al. found J_c greater than 10^4 A/cm² at 4.2 K in 10-25 T of silver-sheathed poly-crystalline tapes of YBCO and $\text{Bi}_2\text{Sr}_2\text{CaCu}_2\text{O}_8$ (BSCCO)³. Furthermore, Murakami from ISETEC had demonstrated the dramatic flux pinning capability of Ag doped YBCO materials from Melt-Powder-Melt-Growth (MPMG) process⁴ by using the processed YBCO

4

pellet to lift a weight of 6 Kg with the repulsive force against a 0.4 T rare earth magnet. Evidently, the addition of silver has apparently improved the overall texture and suppressed cracking in the MPMG processed YBCO materials. In addition, American Superconductor⁵ using internal oxidation of metallic precursor for silver sheathed $\text{Ca}_{0.1}\text{Y}_{0.9}\text{Ba}_2\text{Cu}_4\text{O}_8$ achieved a critical current density of 69,500 A/cm² at 4.2 K in self-field; moreover with an applied field of 0.1 Tesla, the sample retained 39% of its original critical current.

Other aspects of silver and gold with YBCO are also intriguing and have proved that the two interfacial systems deserve more systematic investigation:

1. Silver and gold have been proved to be important contact materials on YBCO⁶ providing the lowest contact resistance to YBCO.
2. Some of the best single crystals of YBCO were made in gold crucible and contain 5 atomic percents Au in substitution of Cu⁷.
3. The nature of the proximity effect, i.e. induced pairing into a normal metal which is in contact with a superconductor, is still illusive. Apparently, a supercurrent can be induced, but not a gap⁸.

To our knowledge, few detailed investigations of the microstructure of the Au/ YBCO interface have been published. Here

we report on the nano-scale structure of the Au/YBCO interface of an over-layer gold film on (001) epitaxial YBCO film. The present study of the nature of the interface with transmission electron microscopy is important to understand the electrical characteristics of the Au/YBCO interface and maybe the Ag/YBCO interface. These two interfaces are technologically important in order to harness YBCO for microelectronic and electrical power applications.

Our present study will investigate the nature of the Au/YBCO interfaces through electron microscopy study. In particular, this study complements our earlier study of the metal/YBCO interfacial properties using X-ray photoelectron spectroscopy, and temperature-dependent contact resistance measurements¹.

Experimental

Films of YBCO were grown on (001) LaAlO₃ at a substrate temperature of 770°C with an oxygen pressure of 200 mTorr by pulsed laser deposition⁹. The base vacuum was first maintained at 4x10⁻⁶ Torr. The energy beam from a YAG laser was frequency quadrupled to give a wavelength of 266nm with an energy density of 2 J/cm² per pulse on the target, while the duration of the pulse was Q-switched to be 4 ns. The deposition rate for YBCO was 0.55 Å/pulse operating at 10 pulses per second. After deposition the chamber was back filled with oxygen, while the substrate was slowly cooled to

100°C. This method has consistently produced YBCO films with a transition temperature of 90K and a critical current of 10^6 A/cm² at 77 K. After the cool-down, without breaking vacuum the overlying Au film was also laser deposited at a rate of 0.15Å/pulse with the background pressure at 4×10^{-6} Torr and the YBCO/LaAlO₃ maintained at 50°C.

Cross-sectional samples were prepared for examination at 400KV in a Jeol-4000FX transmission electron microscope with a coefficient of spherical aberration $C_s=3.4$ mm. Films were glued face-to-face with epoxy and were then cut, polished and dimpled to a thickness not more than 50 micrometer. The samples were then ion-milled with liquid nitrogen cooling at 10 KV Ar ions and finished off with 5 KV Ar ions. Air-exposure was kept to a minimum by keeping sample in desiccator when not being processed. Parts of the Au film were milled away to expose the underlying YBCO film. Details about the preparation of the cross-sectional samples are given elsewhere¹⁰.

Results

The YBCO film examined (see Fig. 1) is a single crystal, epitaxially grown film on the (001) LaAlO₃. The YBCO film is 130nm thick while the overlying gold film is 85nm thick. The gold film is polycrystalline, as is evident from the spotty rings (with the two smallest rings being the {111} and {200} reflections) in the

electron diffraction pattern (see the insert of Figure 1). The gold film is of columnar grain structure with grain size in the film plane close to 5-10 nm, consistent with the low substrate temperature (50°C) used during the Au deposition. Here the electron beam direction is $[110]_{YBCO}$. The satellite spots and the streaking along in the c-direction are from the YBCO film and its high density of stacking faults, translational boundaries and accompanying partial dislocations. The remaining diffraction spots constituting a lattice pattern belongs to the $LaAlO_3$ substrate.

A distinct alloyed layer of 20 nm in the single crystal $LaAlO_3$ under the YBCO film is easily visible. The undulating Au/YBCO interface contrasts to the flat YBCO/ $LaAlO_3$ interface, which suggests that (i) the roughness at the YBCO/Au was not a result of an initial rough $LaAlO_3$ substrate surface and (ii) the final growth stage of the YBCO film was under a condition of large supersaturation and definitely not layer-by-layer like. The maximum peak-to-valley roughness of the YBCO/Au interface is 8 nm, about 7 unit cell height of YBCO, while that of the $LaAlO_3$ /YBCO is 1.7 nm, about 4 unit cell height of $LaAlO_3$ along an interfacial length of 300 nm under observation. Since the coherence length in YBCO is shortest along the c-axis direction, an atomic flat interface of YBCO/Au which is parallel to (001) YBCO will have a much weaker proximity effect than that of any other inclination of the YBCO/Au interface. Steps in the $(001)_{YBCO}$ inclination of the YBCO/Au interface will improve the proximity effect from the otherwise

atomically flat (001) YBCO/Au interface. Control over the interfacial roughness would be desirable to enhance the proximity effect in Au. Here, because of the undulating Au/YBCO interface, effort is required to locate perfect end-on Au/YBCO interfaces for high resolution observation.

All of the interface between the gold and the YBCO film was observed to be well bonded. The interface appears abrupt in the High Resolution Transmission Electron Microscopy (HRTEM) images. No cracks or extraneous phases were observed at the Au/YBCO interface. The interface was always free from extraneous phases as shown in Figures 2 and 3. Although the interface is not always parallel to the (001) planes of the YBCO film, the lattice images of the (001) planes in the YBCO film are continuous and abut at the interface to the gold layer. No array of interfacial dislocations was observed, consistent with the present randomly oriented polycrystalline gold overgrowth. Arrays of interfacial dislocations are usually present at epitaxial interfaces to accommodate the lattice misfit, see the slight strain contrast at the YBCO/LaAlO₃ interfaces (Fig.1). No such lattice matching was apparent here at the Au/YBCO interface, which suggests that the present Au/YBCO interface is completely incoherent, and does not bear any coherent stresses.

Faceting at an atomic scale is obvious in some portions of the Au/YBCO interface where the (001) planes of YBCO are parallel to the interface, so as to maximize the contact area between the (001)

surface of YBCO and the gold layer (Figures 2, 3 and 4). This observation suggests that the (001) YBCO inclination is a low energy interface between gold and YBCO, which is not unexpected giving that the (001) YBCO is a low energy surface. Similar basal plane faceting of $\text{Bi}_2\text{Sr}_2\text{CaCu}_2\text{O}_{8-x}$ (BSCCO) with $T_c=75-95\text{K}$ in contact with silver was also observed where a polytype of a lower transition temperature $\text{Bi}_2\text{Sr}_2\text{Cu}_2\text{O}_{6+x}$ ($T_c=7-22\text{K}$) was observed to form at the steps¹¹. Here, the formation of the $\text{Y}_2\text{Ba}_4\text{Cu}_4\text{O}_{15-x}$ (2-4-8) phase ($T_c=80\text{K}$) at these steps is not regularly observed. When occasionally the translational boundaries with $1/3[001]$ and $2/3[001]$ translation vectors terminate at the (001) atomic steps (Fig. 4). A local half unit cell of the 2-4-8 phase can form under each of these atomic steps, though it is not clear from the present micrograph. Since the stacking fault density is high in the present film, an accidental occurrence of a 2-4-8 phase under one of these steps is a likely event without having special reasons of polytype formation at interface steps. Here, the micrograph (Fig.4) indicates a possibility that these (001) interfacial atomic steps at the Au/YBCO interfaces have halted the migration of these translational boundaries in the YBCO films. These (001) steps have step heights not multiples of the [001] lattice parameter of YBCO but rather the multiples of the one third of the [001] lattice parameter of YBCO. Most of the time, clean steps were observed, as in Figs. 2 and 3, which agrees with the observation¹² of the Ag/YBCO and Au/YBCO interfaces where integral (001) steps were observed without 2-4-8 phase.

It is important to notice that when parts of the YBCO surface were exposed to air or vacuum after the Au over-layer was partly milled away as shown in Fig. 5, the (001) lattice fringes of the YBCO stop at about 10 nm away from the surface. Presumably, there exists an amorphous layer right under the surface (denoted as region A in Fig.5). However, under the remaining gold layer, the (001) lattice fringes of YBCO again terminate abruptly at the Au/YBCO interface (denoted as region B). This indicates that gold is a good surface passivation for the underlying YBCO film, preventing reactions and amorphorization.

The well-bonded interfaces between the overgrown gold film and the underlying epitaxial YBCO film, together with the fact that the interface always appears free of extraneous phases, which support the general view that Au is a desirable contact material to the YBCO film for various applications requiring low contact resistance^{13, 14, 15} as well as a dependable surface passivation layer for YBCO. Our results give clues of the other possible good interfaces between Au/other superconducting cuprates as well as Ag/YBCO because of the iso-electric similarity between Au and Ag, and among the superconducting cuprates. From the present results and earlier observations^{11, 12}, basal plane faceting is frequently observed at the interfaces of superconducting cuprates with silver and gold.

Conclusions

We have investigated the structure of the interfaces in term of the presence of extraneous phases, degree of coherency, and interface step content across the interfaces. Our present microstructural results agree with our earlier studies of the Au /YBCO interfacial properties using X-ray photoelectron spectroscopy, and temperature dependent contact resistant measurements¹.

Acknowledgements

S.-W. C. thanks Dr. C. Chen for her technical assistance. S.-W. C. acknowledges the support from the Air Force Office of Scientific Research, under grant F49620-92-J-0160. Q. L. and D. B. F. acknowledge support by the Department of Energy (DE-FG01-90-ER81084), National Science Foundation (ISI-9160506), and the Air Force Office of Scientific Research, under grant F49620-93-C-0010).

Figure Captions

1. Low magnification transmission electron micrograph showing (i) the (001) LaAlO_3 substrate, (ii) the epitaxial YBCO film of (001) orientation with 130 nm in thickness as well as (iii) the overlying, polycrystalline gold film of 85 nm in thickness. Note the 20 nm alloyed layer underneath the YBCO film in LaAlO_3 . The insert is an electron diffraction pattern from the area (see text more detail).
2. High Resolution Electron Micrograph of the YBCO/Au interface showing 5 integral steps, each of a height corresponding to $[001]_{\text{YBCO}}$ at the interface (left side) and a large portion of an interface parallel to the (001) plane of YBCO (right side).
3. High Resolution Electron Micrograph of the YBCO/Au interface showing integral $[001]_{\text{YBCO}}$ steps at the interface and the local roughness of the interface (i.e. not end-on) affecting the observation of the interface.
4. High Resolution Electron Micrograph of the YBCO/Au interface showing non-integral $[001]_{\text{YBCO}}$ interfacial steps where the translational boundaries in YBCO terminated.
5. Part of the YBCO surface exposed to air/vacuum after the Au over-layer was milled away. Region A: missing lattice fringes

of the (001) planes under the YBCO surfaces where the gold had been milled away. Region B: the (001) lattice planes of YBCO ended at the interface with the gold over-layer.

REFERENCES

1. Q.Y. Ma, M.T. Schmidt, L.S. Weinman, E. S. Yang, S. M. Sampere, and Siu-Wai Chan, *J. of Vacuum Science and Technology A*, **9**, 390 (1991).
2. K. Heine, J. Tenbrink, and M. Thoener, *Appl. Phys. Lett.* **55**, 2441-2443 (1989).
3. K. Osamura, T. Takayama, and S. Ochiai, *Superconductor Sci. Technol.* **2**, 107 (1989).
4. M. Murakami, *Flux Pinning of Melt Processed YBCO Superconductors and Their Applications*, to be published in studies of High Temperature Superconductors, ed. A. V. Narikar, (Nova Science Publishers, Tokyo, 1991).
5. L. J. Masur, E. R. Podtburg, C. A. Craven, A. Otto, Z. L. Wang, D. M. Kroeger, J. Y. Coulter and M. P. Maley, preprint submitted to *Physica C* March 1994.
6. Y. Tzeng, A. Holt, and R. Ely, *Appl. Phys. Lett.* **52**, 155 (1988), and J. W. Ekin, A. J. Panson, and B. A. Blankenship, *Appl. Phys. Lett.* **52**, 331 (1988). and J. W. Ekin, T. M. Larson, N. F. Bergen, A. J. Nelson, A. B. Swartzlander, L. L. Kazmerski, A.J. Panson, and B. A. Blankenship, *Appl. Phys. Lett.* **52**, 1819 (1988).
7. D. L. Kaiser, F. Holtzberg, M. F. Chisholm, and T. K. Worthington, *J. of Crystal Growth*, **85** 593 (1987).
8. P. M. Mankiewich, D. B. Schwartz, R. E. Howard, L. D. Jackel, B. L. Straughn, E. G. Burkhardt, and A. H. Dayem, 5th

International Workshop on Future Electron Devices-- High Temperature Superconducting Electron Devices-(FED HiTcSc-ED WORKSHOP), June 2-4, 1988, MIyagi-ZAo, pp. 157-160; P.M. Mankiewich, et al, IEEE-Magnetic, 25, (1990); L. H. Greene et.al. Physica C 162-164, 1573 (1989); R. H. Ono, J. A. Beall, M. W. Cromar, T. E. Harvey, M. E. Johansson, C. D. Reintsema and D. A. Rudman, Appl. Phy. Lett. 59 1126 (1991).

9. Q. Li, D. B. Fenner, W. D. Hamblen and D. G. Hamblen, Appl. Phy. Lett. 62, 2428 (1993). D. B. Fenner, Q. Li, W. D. Hamblen, M. E. Johansson, D. G. Hamblen, L. Lynds, and J. I. Budnick, IEEE Trans, Appl. Supercon. 3, 2104 (1993).
10. Siu-Wai Chan, D. M. Hwang, L.Nazar, J. Appl. Phys. 65 4719 (1989).
11. Y. Feng, D. C. Larbalestier, S. E. Babcock, and J. B. Vander Sande, Appl. Phys. Lett. 61 1234 (1992).
12. A. F. Marshall, and R. Ramesh, in "Interfaces in High-T_c Superconducting Systems", edited by S. L. Shinde and D. A. Rudman (Springer-Verlag, New York, 1994) p. 71.
13. V. Pendrick, R. Brown, J. R. Matey, A. Findikoglu, X.X. Xi, T. Venkatesan, and A. Inam, J. Appl.Phys. 69 7927 (1991).
14. J. W. Ekin, S. E. Russek, C.C. Clickner, and B. Jeanneret, Appl. Phys. Lett. 62 369 (1993).
15. Contact resistivity¹ of Au/YBCO interfaces from an ex-situ process was reported to be $8.6 \times 10^{-3} \Omega \text{ cm}^2$ at 300K and $4.9 \times 10^{-5} \Omega \text{ cm}^2$ at 77K, while a lower value¹³ of $2.6 \times 10^{-7} \Omega \text{ cm}^2$ at 79K with oxygen anneal from an ex-situ process and even a lower

contact resistivity¹⁴ in the range of 10^{-8} - 10^{-9} Ω cm² at 4K from an in-situ process without oxygen anneal had been reported.



Fig. 1

11

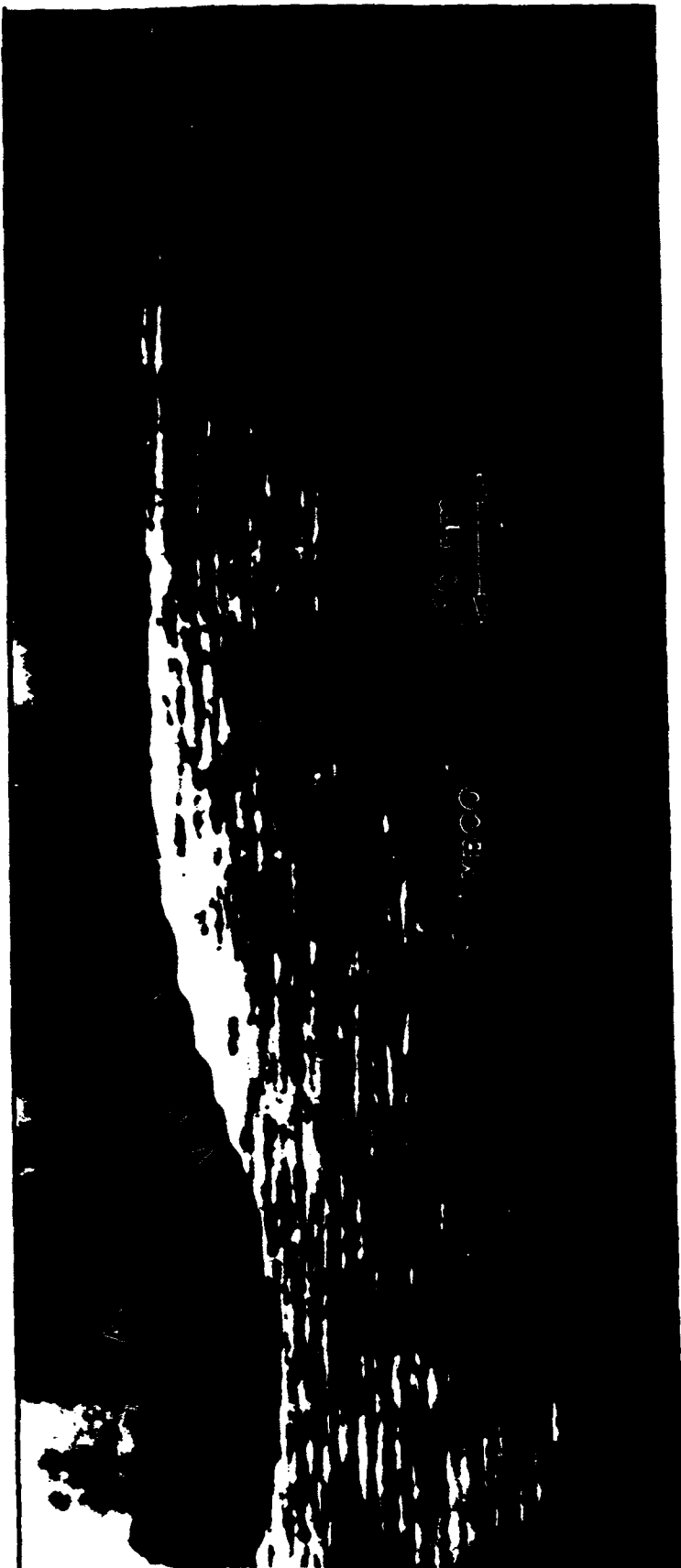


Fig. 2

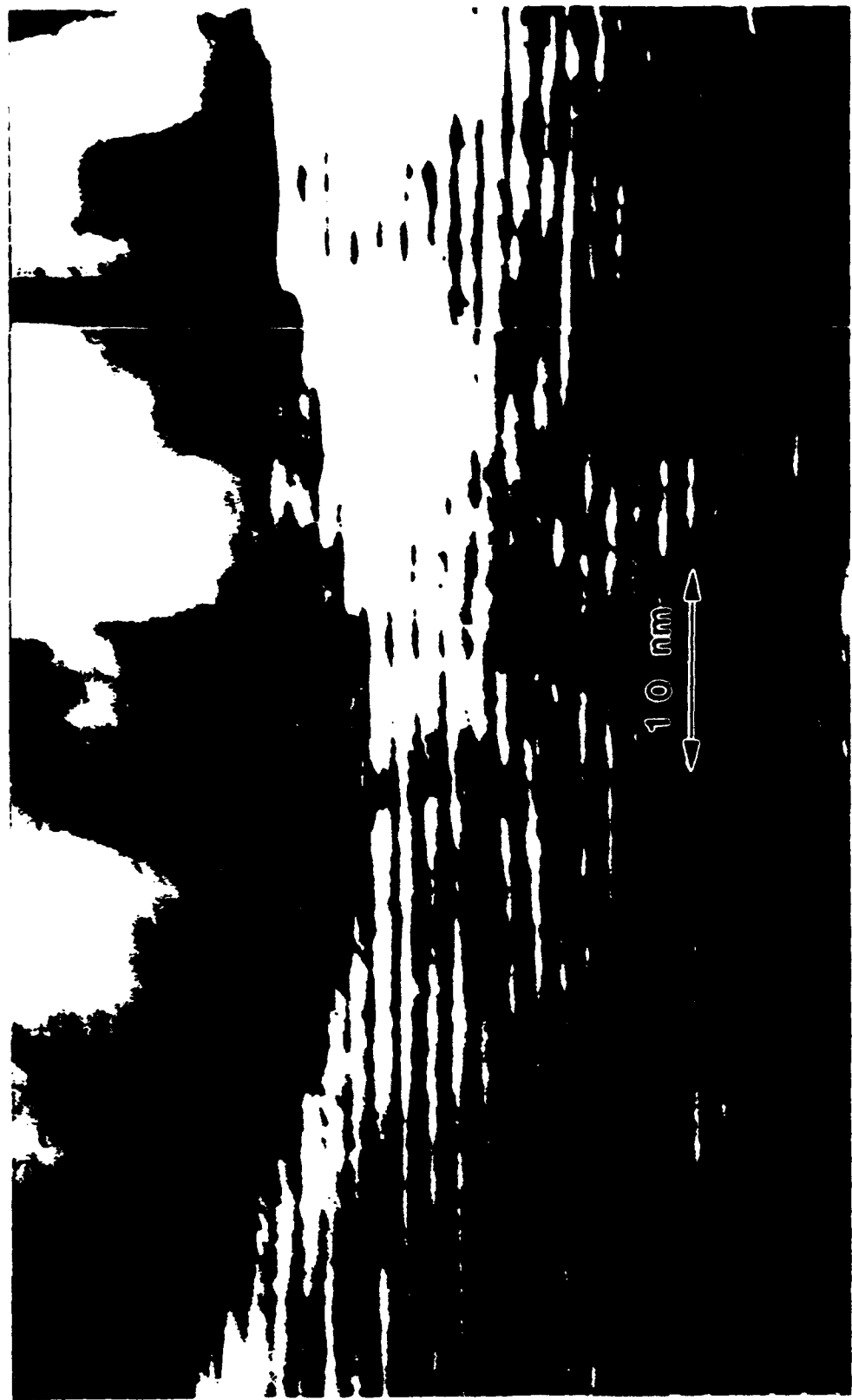


Fig. 3.



Fig 4

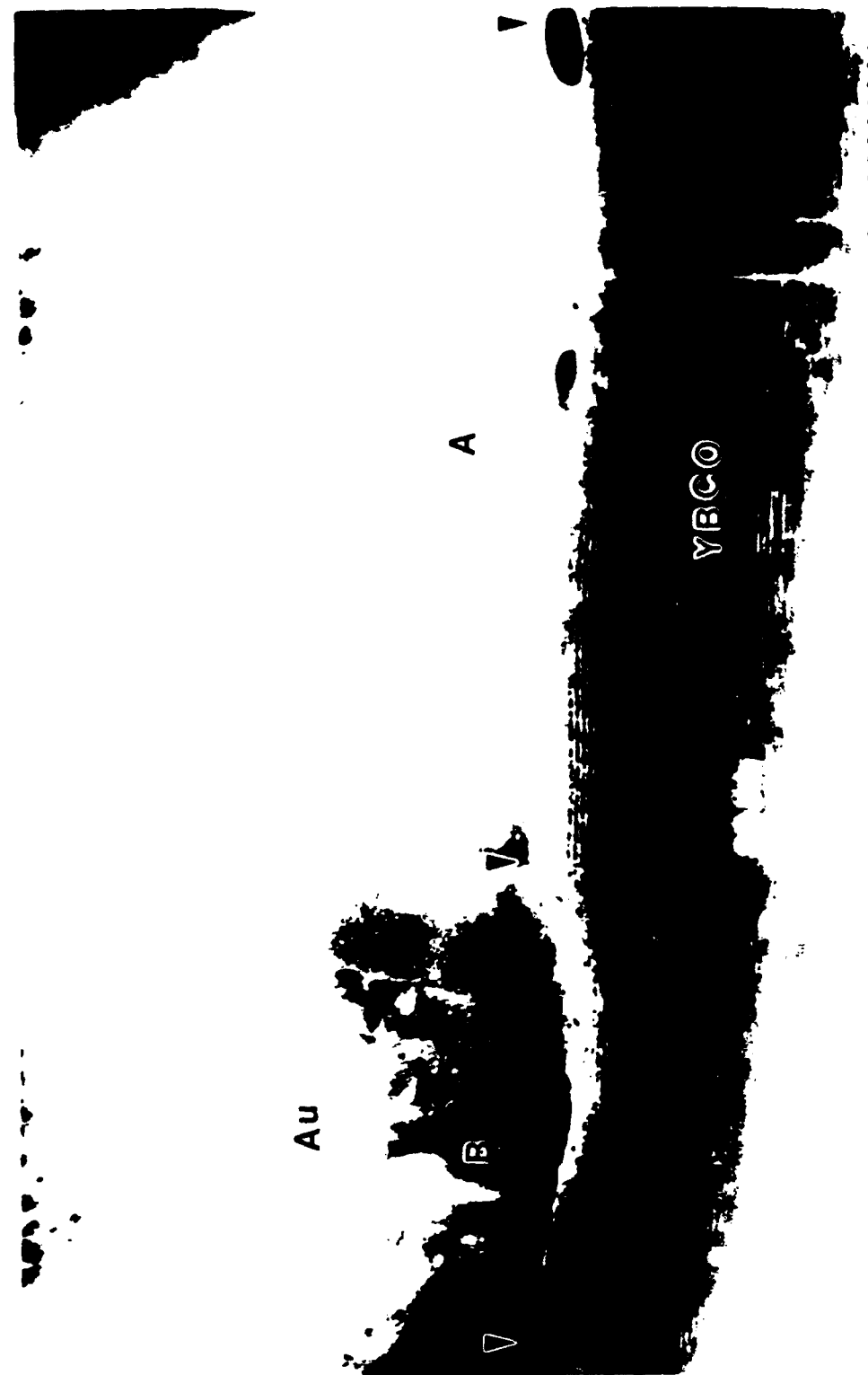


Fig. 5

The critical current density in high fields in epitaxial thin films of $\text{Y}_1\text{Ba}_2\text{Cu}_3\text{O}_{7-\delta}$: Flux pinning and pair breaking

D. P. Hampshire

Department of Physics, Durham University, South Road, Durham, DH1 3LE, United Kingdom

Siu-Wai Chan

Columbia University, Henry Krumb School of Mines, Materials Science Division, New York, New York 10027

(Received 4 March 1992; accepted for publication 23 June 1992)

The critical current density (J_c) of two epitaxial thin films of $\text{Y}_1\text{Ba}_2\text{Cu}_3\text{O}_{7-\delta}$ has been measured as a function of temperature in magnetic fields up to 27 T. A detailed study of one of the films shows that when the transport current is in the a - b plane and the magnetic field is *orthogonal* to the c axis, the functional form of J_c is consistent with both a polynomial (flux pinning) description and an exponential (pair breaking) description. In contrast, when the current is in the a - b plane and the applied field is *parallel* to the c axis of the film, J_c is unambiguously exponential of the form $J_c = \alpha(T) \exp[-\mu_0 H/\beta(T)]$. These results explain why there are conflicting suggestions in the literature as to the mechanism that determines J_c in high magnetic fields in thin films for $J \parallel H \parallel c$ axis and provide evidence that pair breaking operates for $J \perp H \parallel c$ axis. However, the standard phenomenological superconductor-normal-superconductor junction model derived in the clean limit for the normal metal cannot describe this pair-breaking mechanism.

I. INTRODUCTION

Many authors have reported large critical current densities in epitaxial $\text{Y}_1\text{Ba}_2\text{Cu}_3\text{O}_{7-\delta}$ thin films.¹⁻⁴ Two distinctly different mechanisms have been proposed to explain the magnetic field dependence, temperature dependence and anisotropy of J_c : a flux pinning mechanism⁵⁻⁸ and a pair-breaking mechanism.^{9,10} This lack of agreement precludes us from identifying the best route for optimising the fabrication of thin films. For example, in principle, in order to increase J_c : if a flux pinning mechanism is operating, we must add pinning sites; if pair breaking operates, we must identify the regions where pair breaking is occurring and remove them.

We have measured the critical current density in very high magnetic fields up to 27 T from 4.2 K up to T_c of two epitaxial thin films of $\text{Y}_1\text{Ba}_2\text{Cu}_3\text{O}_{7-\delta}$ deposited on single crystal (001) SrTiO_3 substrates. By obtaining measurements of J_c over a wide temperature range in magnetic fields up to 27 T, we clarify why there are conflicting suggestions as to the mechanism limiting J_c in high magnetic fields and address whether a flux pinning mechanism or a pair-breaking mechanism operates.

II. SAMPLE PREPARATION

The two epitaxial thin films were prepared by the co-evaporation of Y, BaF, and Cu from three separate sources onto the (001) surface of a single crystal of SrTiO_3 .¹¹ The barium fluoride and the yttrium were evaporated using electron-beam guns while the copper was evaporated using a resistively heated source. The films were subsequently annealed at 850 °C in flowing oxygen to form the $\text{Y}_1\text{Ba}_2\text{Cu}_3\text{O}_{7-\delta}$ phase.

A detailed transmission electron microscopy study of the microstructure of similar films to these has demon-

strated that these films are strongly textured. The majority of the film is oriented with the c axis of the orthorhombic structure orthogonal to the film surface and the a axis parallel to either the (100) or (010) directions of the SrTiO_3 . However there is a threefold degenerate epitaxy of the $\text{Y}_1\text{Ba}_2\text{Cu}_3\text{O}_{7-\delta}$ on the SrTiO_3 substrate. Hence grains having typical dimensions of $4 \mu\text{m} \times 20 \mu\text{m}$ with their c axis parallel to either (100) or (010) directions of the SrTiO_3 are also present.^{11,12} These grains occupy less than 5% of the area of the film.

Both films were patterned using laser ablation. The thickness of each film was determined using Rutherford backscattering. On the first film which was $1 \mu\text{m}$ thick, two bridges were patterned (A and B). The second film was $0.25 \mu\text{m}$ thick and had a single bridge (C) patterned onto it. Table I lists the dimensions of these bridges as well as the configuration of J , H , and the c -axis of the film for the data presented in this article.

III. EXPERIMENTAL DETAILS

A. Critical current density measurements

We performed standard four terminal resistive and J_c measurements using a variable temperature insert.¹³ Electrical contact was made via gold pads which were evaporated onto the film.¹⁴ Zero resistivity for these films was obtained at about 87 K.

The critical current measurements were made using a variable temperature insert. In zero magnetic field the temperature was fixed at that required using a heater and a calibrated carbon glass thermometer. A field-independent strontium titanate thermometer was then used in closed loop with the heater to keep the temperature constant while measuring the voltage-current characteristic in high

TABLE I. Dimensions of the bridges and the configurations of J , H , and c axis for the data in Figs. 1–11 (J_{lc} for all bridges).

Bridge	Dimensions/		Film	Figure	Orientation of J , H , and c axis
	μm (length × width)	μm Thickness/			
A	15 × 5	1.00	1	1	$H \perp c$, $H \parallel J$
				5	$H \perp c$, $H \parallel J$, and $H \parallel J$
				6	$H \perp c$, $H \parallel J$
				8	$H \perp c$, $H \parallel J$
B	60 × 20	1.00	1	2	$H \perp c$, $H \parallel J$
				9	$H \perp c$, $H \parallel J$
C	45 × 15	0.25	2	3	$H \perp c$, $H \parallel J$
				4	$H \parallel c$
				7	$H \parallel c$
				10	$H \parallel c$ and $H \perp c$, $H \parallel J$
				11	$H \parallel c$ and $H \perp c$, $H \parallel J$

magnetic fields. The uncertainty in temperature for these data is about 4%.

In Figs. 1 and 2 the critical current density as a function of field and temperature is presented for each of the bridges on film 1. The smooth curves shown at each temperature serve as aids to the eye. In both figures the data were obtained when the magnetic field and the current flow direction were in the plane of the film. The transport current was orthogonal to the applied field (i.e., $J \perp H \perp c$ axis) hence there was a net Lorentz force. The voltage criterion used to define J_c was 1 μV . This criterion was chosen at a value sufficiently low to avoid any problems due to sample heating and yet obtain good signal to noise.

In Fig. 1 above 40 K, there are two distinct regimes in the J_c vs H curve at each temperature. Over the intermediate magnetic field range J_c gradually and smoothly decreases as the magnetic field increases. Eventually there is a pronounced steep decrease in J_c at the highest field level. It should be noted that when J_c is less than 1 mA, the sample is resistive. Hence the drop in J_c at the highest magnetic field level would be steeper and the cross-over from one regime to the other even more pronounced were

J_c defined at a lower voltage criterion. At 40 K and below, since the data is restricted to magnetic fields up to 20 T, we can only access the intermediate magnetic field regime. The J_c data in Fig. 2 has a similar magnetic field dependence at each temperature to that in Fig. 1. However the magnitude of J_c in bridge B is about a factor of three smaller at low temperatures and an order of magnitude smaller at higher temperatures.

The critical current density of bridge C (film 2) as a function of field and temperature is presented in Figs. 3 and 4. The data in Fig. 3 were obtained with the same configuration of magnetic field and current flow used to obtain the data in Figs. 1 and 2. However in Fig. 4, although J remains in the a - b plane the applied field is *orthogonal* to the face of the film (i.e., $H \parallel c$ axis). J_c is defined at a criterion of 1 μV . The error bars in these figures describe the change in J_c when the voltage criterion is changed. The upper bound of the error bar is the J_c value when the voltage criterion is 2 μV . The lower bound is the J_c value found by a linear extrapolation through 2 μV and 1 μV to zero μV .

Although the data in Fig. 3 are only obtained in magnetic fields up to 14 T, they show a similar functional form to the data in Figs. 1 and 2 over the same field and temperature range. The similarity in the field and temperature dependence of the critical current density is consistent with the nominally identical fabrication procedure for the two films. We expect that the difference in the magnitudes of J_c that does occur is primarily due to small compositional differences between the three bridges although we have not completed a detailed systematic study of the composition of these films.

In Fig. 4 where the film is oriented such that $H \parallel c$ axis, there is a markedly different functional form for the field dependence of J_c at each temperature to that found in the previous figures. In Figs. 1, 2, and 3 over the intermediate magnetic field range, there is only a small change in J_c at each temperature (typically less than half a decade). However in Fig. 4, the decrease in J_c as the magnetic field increases is much larger. For example, at 20 K, J_c de-

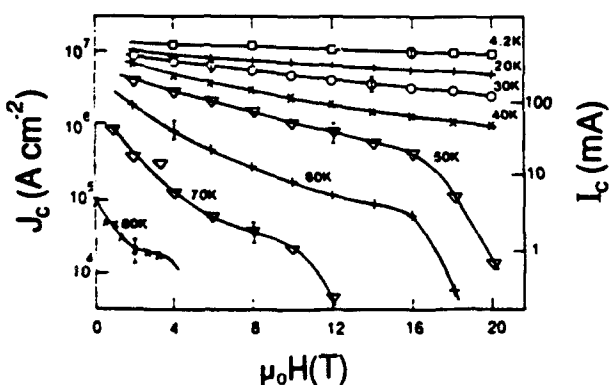


FIG. 1. The critical current density defined at 1 μV as a function of field and temperature for bridge A on film 1. J is orthogonal to the c axis. The applied field is orthogonal to both J and the c axis.

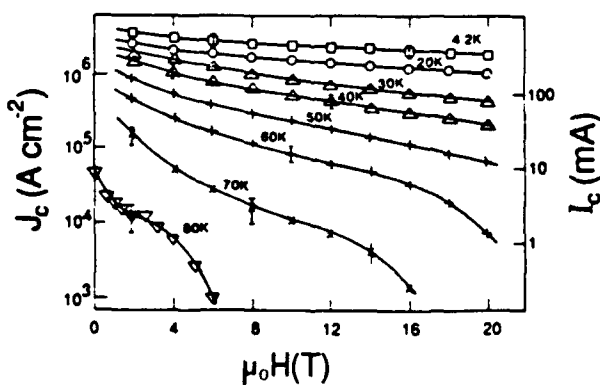


FIG. 2. The critical current density defined at 1 μV as a function of magnetic field and temperature for bridge B. J is orthogonal to the c axis. The applied field is orthogonal to both J and the c axis.

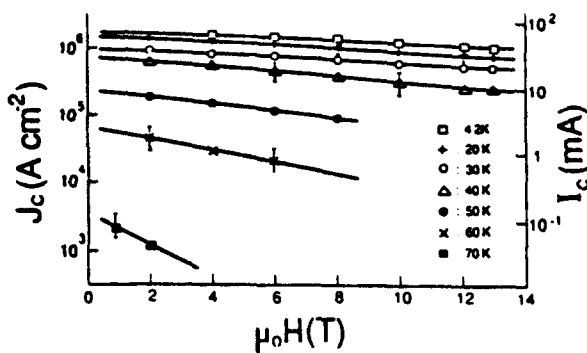


FIG. 3. The critical current density defined at 1 μ V as a function of field and temperature for bridge C. J is orthogonal to the c axis. The applied field is orthogonal to both J and the c axis.

creases exponentially over nearly four orders of magnitude in applied magnetic fields up to 27 T.

B. Orientation dependence of J_c

In Fig. 5 the orientation dependence of J_c is considered for bridge A. J_c was measured at 20 and 40 K in applied fields up to 20 T. In both configurations J and H are parallel to the face of the film. For $J \parallel H$ a net Lorentz force operates, whereas there is no net Lorentz force for $J \perp H$. Despite the large difference in the net Lorentz force between the two configurations, there is less than a factor of two difference between J_c for the two orientations. A similarly weak dependence on the relative orientation of the critical current density and the magnetic field was found over the same field and temperature range as that presented in Fig. 5 for bridge B.

C. Differential resistivity

Much experimental and theoretical work has addressed the dissipative mechanisms that operate during flux motion in superconducting materials and in particular the differential resistivity above J_c .¹⁵⁻¹⁹ In Fig. 6 the differential resistivity calculated over the range from 1 to 5 μ V is presented as a function of field and temperature for

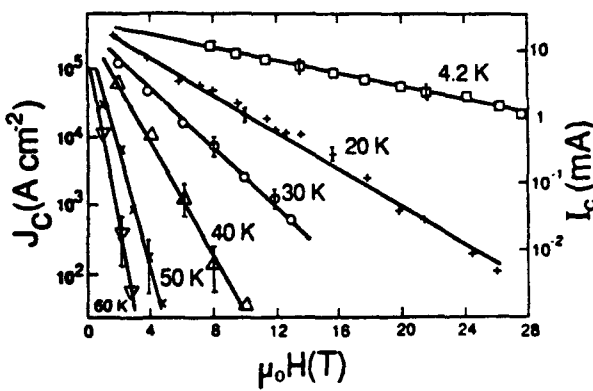


FIG. 4. The critical current density defined as a function of field and temperature for bridge C. J is orthogonal to the c axis of the film. The applied field is parallel to the c axis.

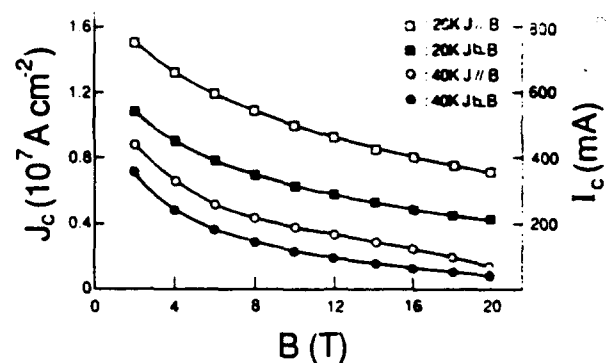


FIG. 5. The critical current density as a function of magnetic field at 20 and 40 K for J parallel (zero net Lorentz force operating) and orthogonal (Lorentz force operating) to the applied field for bridge A. In both configurations the applied field is orthogonal to the c axis of the film.

bridge A, where $J \parallel H \parallel c$ axis. The trends found in Fig. 6 are also found for this orientation of J and H both for bridge B and bridge C. In Fig. 7, ρ_1 is presented for the second film when $H \parallel c$ axis (i.e., calculated from the raw V - I traces used to generate the data in Fig. 4). It should be noted that in Figs. 6 and 7, ρ_1 is an increasing function of magnetic field and temperature.

IV. ANALYSIS OF DATA

A. Pinning and pair breaking

In the analysis below we explicitly consider whether our data can be used to distinguish between whether a pinning or a pair-breaking mechanism has determined J_c .

When the volume pinning force ($F_p = J_c \times B$) is of the Fietz-Webb separable variable form²⁰ given by

$$F_p = \gamma B_{c2}^n(T) f(b)$$

[where γ is determined solely by the physical properties of the film, $B_{c2}(T)$ is the upper critical field, and $f(b)$ is a function only of the reduced magnetic field $b = B/B_{c2}(T)$], this dependence provides evidence that a flux pinning

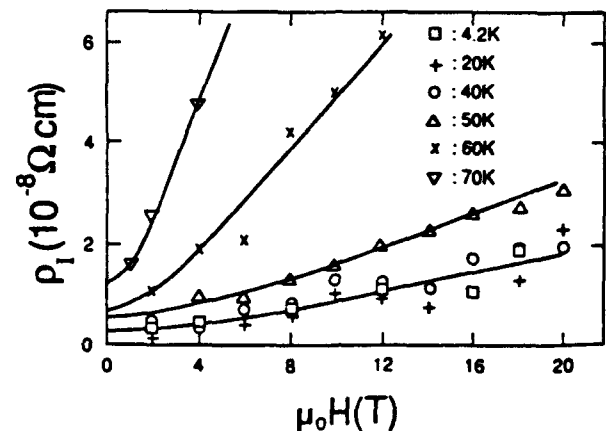


FIG. 6. The differential resistivity defined over the range from 1 to 10 μ V as a function of magnetic field and temperature for bridge A. J is orthogonal to the c axis. The applied field is orthogonal to both J and the c axis.

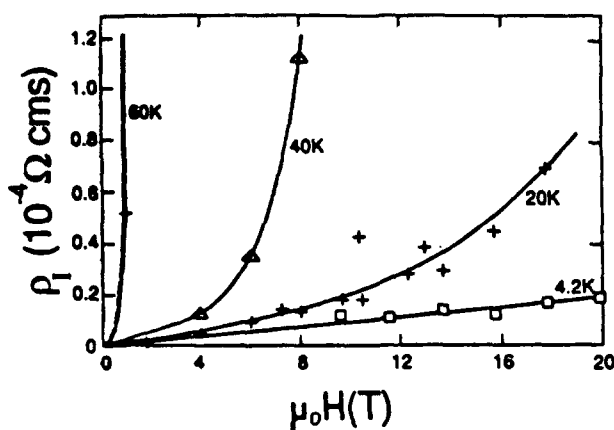


FIG. 7. The differential resistivity defined over the range from 1 to 5 μ V as a function of magnetic field and temperature for bridge C. J is orthogonal to the c axis. The applied field is parallel to the c axis of the film.

mechanism limits J_c . The volume pinning force of many superconducting materials is described by this scaling law and the values of γ , n , and the functional form of $f(b)$ are used to identify which pinning mechanism is operating.²¹⁻²³

Alternatively we can consider the role of the proximity effect where the critical current density is determined by pair-breaking perturbations (e.g., magnetic impurities, regions of low T_c). The work of De Gennes on normal/superconducting boundaries²⁴ shows that the superconducting order parameter can decay exponentially in the normal barrier such that in a superconducting/normal metal/superconducting junction for both a dirty superconductor and a clean superconductor close to T_c ,

$$J_c(T) = J_0(1 - T/T_c)^2 \exp(-K_n d_n),$$

where J_0 is a constant, d_n is the thickness of the normal layer and K_n^{-1} is the characteristic decay length for the superconducting order parameter in the normal layer. Hsiang and Finnemore²⁵ have extended this work by including the magnetic field dependence of K_n and shown that when the normal metal is in the clean limit:

$$J_c(B, T) = \alpha(T) \exp[-\mu_0 H/\beta(T)] \quad (1)$$

[where $\alpha(T)$ and $\beta(T)$ are functions of temperature alone].

1. H_{c2} axis, $J \perp H$

In Figs. 8 and 9, the volume pinning force is presented as a function of field at temperatures of 40 K and above for the two bridges on film 1. In both figures, the data show a very weak magnetic field dependence at each temperature over the intermediate field range. An important feature of the data in Fig. 8 (or equivalently Fig. 1) is the marked steep drop of F_p (or J_c) in the highest magnetic fields at each temperature. We can associate the magnetic field at which this transition occurs as the effective upper critical field $B_{c2*}(T)$.²⁶ Having explicitly measured $B_{c2*}(T)$, we can analyze the data in Fig. 8 within the framework of the Fietz-Webb scaling law.²

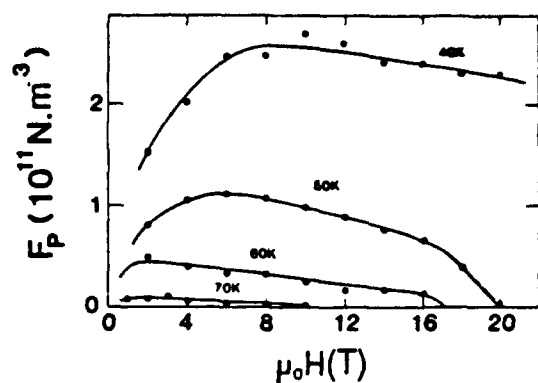


FIG. 8. The volume pinning force as a function of field and temperature for bridge A on film 1. J is orthogonal to the c axis. The applied field is orthogonal to both J and the c axis.

In the standard Fietz-Webb analysis, the values for γ and n are calculated by considering the temperature dependence of the maximum pinning force.^{20,21,23} This analysis is not appropriate here for the data shown in Fig. 8. We have taken F_{p*} at $0.5B_{c2*}(T)$ (i.e., F_{p*}) as a value characteristic of the intermediate magnetic field range at each temperature [where $B_{c2*}(T)$ at 50, 60, 70, and 80 K are taken to be 4.8, 12, 18, and 21 T, respectively]. Above 40 K, F_{p*} can be described by a Fietz-Webb scaling law of the form

$$F_{p*} = \gamma^* B_{c2*}^n(T)$$

[where $\gamma^* = 6.3 \times 10^5 \text{ N m}^{-3}$ and $n = 3.8 \pm 1.3$].

A weak magnetic field dependence for F_p has been observed previously in $\text{YBa}_2\text{Cu}_3\text{O}_{7-\delta}$ ²⁷ as well as in the low temperature superconductor V_3Ga ²⁸ in which a flux pinning mechanism is expected to operate. The temperature dependence of F_{p*} is also similar to that found in V_3Ga where the index n was found to be about 3. In summary we find that the field and temperature dependence of J_c for bridge A above 40 K over the intermediate magnetic field range can be described within the Fietz-Webb framework. Since the functional form of J_c is similar in Figs. 1-3,

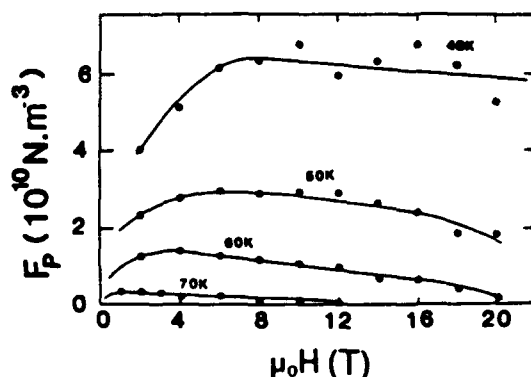


FIG. 9. The volume pinning force as a function of field and temperature for bridge B. J is orthogonal to the c axis. The applied field is orthogonal to both J and the c axis.

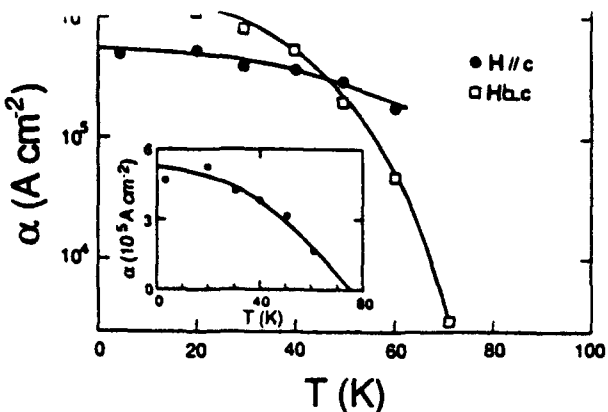


FIG. 10. $\alpha(T)$ as a function of temperature for film 2 for both the applied field parallel to the c axis (●) and the applied field orthogonal to the c axis (□). The current direction is along the a - b plane and orthogonal to the field. [Inset: $\alpha(T)$ vs T for $H \parallel c$ axis. The curve drawn through the data points is given by $\alpha(T) = 5.2 \times 10^5 [1 - (T/75)^2]$.]

it is clear that the data in Figs. 2 and 3 can also be described within the framework of the Fietz-Webb analysis.

Alternatively, we can consider whether a pair-breaking mechanism is consistent with the data in Figs. 1, 2, and 3. A preliminary inspection of the data in these log-linear figures shows that over most of the magnetic field range, J_c can be described reasonably well by an exponential of the form given in Eq. (1).

In summary for $H \parallel c$, above 40 K over the intermediate magnetic field range, the functional form of J_c in these films is consistent with both a Fietz-Webb flux pinning description and an exponential pair-breaking description.

2. $H \parallel c$ axis, $J \perp H$

From Fig. 4 where $H \parallel c$ axis, it is clear that J_c can be expressed in the form

$$J_c = \alpha(T) \exp[-\mu_0 H / \beta(T)].$$

Since J_c is exponential over nearly four orders of magnitude at fixed temperature, we rule out an equivalent simple polynomial to describe the functional form of J_c in this orientation. Hence unlike the data in Figs. 1, 2, and 3, the functional form of J_c in Fig. 4 is not consistent with the standard flux pinning law.

In Figs. 10 and 11, the functional form of $\alpha(T)$ and $\beta(T)$ are presented. From the insets of Figs. 10 and 11, we find $\alpha(T) = 5.2 \times 10^5 [1 - (T/75)^2] \text{ A cm}^{-2}$ and for $T > 20 \text{ K}$, $\beta(T) = 1.25 \times 10^3 \text{ T}^{-2}$. It is of note that a decrease in $\beta(T)$ as the temperature increases has been observed quite generally.^{9,29,30}

Many authors have suggested that the pair-breaking mechanism is a S - N - S junction behavior.^{9,10} We now consider whether a simple S - N - S model that assumes a normal barrier orthogonal to the a - b plane can describe the pair-breaking mechanism. In the standard S - N - S model²⁵:

$$\beta(T) = \hbar / (2\sqrt{3}eIld), \quad (2)$$

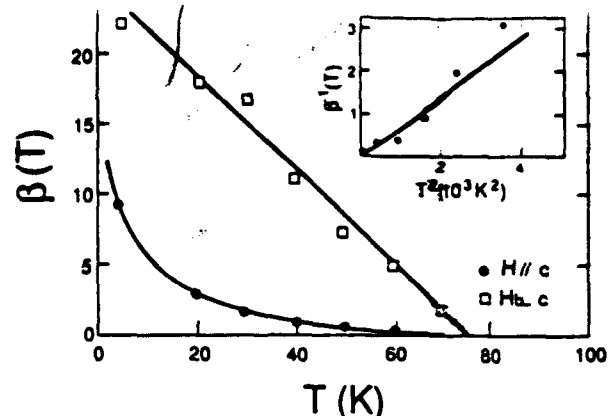


FIG. 11. $\beta(T)$ as a function of temperature for the applied field parallel to the c axis (●) and the applied field orthogonal to the c axis (□). The current direction is along the a - b plane and orthogonal to the field. [Inset: $\beta(T)^{-1}$ vs T^2 for $H \parallel c$.]

where $\hbar = h/2\pi$ (h is Planck's constant), e is the electronic charge, I is the electron scattering length in the normal barrier, and d is the width of the barrier. In S - N - S junctions fabricated with low temperature superconductors, below T_c where I is independent of temperature, $\beta(T)$ is independent of temperature in agreement with Eq. (2). At the higher temperatures investigated in this work, it is reasonable to allow the possibility that since I may decrease, $\beta(T)$ may increase as the temperature increases. However we have found quite the opposite temperature dependence, namely that $\beta(T)$ decreases as the temperature increases. In conclusion although the exponential functional form of J_c suggests a pair-breaking mechanism for $H \parallel c$, within the framework of the standard S - N - S model, normal barriers in the clean limit that are orthogonal to the a - b plane cannot explain the temperature dependence for $\beta(T)$.

In Figs. 10 and 11, values for $\alpha(T)$ and $\beta(T)$ are also presented that have been calculated using the data in Fig. 3 where $H \parallel c$ axis. We find again that $\beta(T)$ decreases as the temperature increases. Hence given that we cannot distinguish whether a flux pinning mechanism or a pair-breaking mechanism operates in this orientation, in the event that the mechanism is pair breaking, the simple phenomenological S - N - S model cannot describe the temperature dependence of these data.

B. Differential resistivity

Theoretical calculations that consider the synchronous motion of the entire flux-line lattice across an isotropic superconductor predict that ρ_1 should be proportional to the applied magnetic field and hence intercept at the origin.^{15,16,31} Physically this proportionality can be associated with dissipation occurring throughout the entire flux-line lattice. In contrast in a granular system where dissipation occurs at the barriers, we expect a nonzero intercept for ρ_1 at $H=0$.^{32,33} Hence in principle, we can use ρ_1 to investigate the nature of any granularity in films.

Unfortunately the data in Figs. 6 and 7 are not conclusive in determining whether granularity plays a signif-

cant role in these films. The increase in ρ_i for increasing magnetic field or temperature is similar to that found in the low temperature superconductors NbTi,¹⁸ Nb₃Sn,³⁴ and V₃Ga²⁸ (i.e., nongranular materials). In addition, at each temperature over much of the intermediate field range the data are consistent with ρ_i being proportional to the applied magnetic field. This proportionality can be interpreted as implying that at criticality (i.e., $J=J_c$), flux is moving throughout the entire film. However, the solid lines in Fig. 6 provided as a guide to the eye demonstrate that these differential resistivity data are not sufficiently detailed to rule out a large nonzero intercept value for $\rho_i(H=0)$. In order to use ρ_i as a diagnostic to identify granularity, we need a better theoretical understanding of this parameter and detailed accurate data in the experimentally demanding high- J_c region close to $H=0$.

C. Orientation dependence

The weak dependence on the relative orientation of the macroscopic current density flow and the applied magnetic field for $H \parallel c$ axis is consistent with a large distribution in the local critical current density throughout the sample. Both a granular system and a system with a large distribution in flux pinning satisfy this description. The factor of 2 change in J_c found in Fig. 5 is more typical of a granular system³⁵ than a nongranular flux pinning system (for which factors of 5 are typical³⁶). Nevertheless, factors equal to and less than 2 have been observed in systems limited by flux pinning.³⁷ Since the very short coherence length^{38,39} and the nonmetallic bonding⁴⁰ in Y₁Ba₂Cu₃O_{7- δ} can cause a broad distribution in the flux pinning properties and/or granularity in these films, the weak orientation dependence of J_c cannot be used to distinguish a system limited by flux pinning from one limited by pair breaking.

V. DISCUSSION

A number of authors have described J_c data within the Fietz-Webb pinning framework. In general the effective upper critical field has been calculated by extrapolating J_c parabolically to zero.^{2,8} For $H \parallel c$ we have found that this extrapolation procedure does not correctly describe J_c —since J_c decreases exponentially. Given that the functional form of J_c derived is not valid throughout the entire superconducting phase, it cannot be considered as evidence that a flux pinning mechanism limits J_c .

The interpretation of data describing the anisotropy of J_c remains ambiguous. Some authors conclude that twin boundaries or stacking faults are responsible for the functional form of J_c ,^{6,7} whereas others suggest that the role of microstructure in their films is negligible.⁴¹ As such the effect of the microstructure on J_c is unclear.

For $H \parallel c$, in common with other authors, we have found that J_c drops to zero at an effective upper critical field $B_{c2*}(T)$ that is well below the accepted values for the thermodynamic upper critical field.^{42,43} A distribution in the fundamental parameters^{13,44,45} flux-line lattice melting,⁴⁶ and depinning^{47,48} have all been suggested as mech-

anisms to describe $B_{c2*}(T)$ (or equivalently the irreversibility line). The discrepancy between $B_{c2}(T)$ and $B_{c2*}(T)$ (which is not significant in the low temperature superconductors) remains a stumbling block in our understanding of J_c in high temperature superconductors. Theoretical descriptions of pinning which include intrinsic pinning, collective pinning, thermal activation and the anisotropy of these materials are being developed.⁴⁹⁻⁵³ Nevertheless, there is no consensus as to the best framework within which to consider J_c data.

The simple phenomenological model for a $S-N-S$ barrier does not describe the magnetic field and temperature dependence of K_n —or equivalently the temperature dependence of $\beta(T)$ —found experimentally for $H \parallel c$. However the exponential magnetic field dependence of J_c provides evidence that the proximity effect plays an important role and hence depairing is the mechanism limiting J_c in this orientation. Until the location and nature of the regions of pair breaking are identified we cannot have a detailed theoretical understanding of K_n .

Direct observation of the flux-line lattice and theoretical modeling of these strongly anisotropic (or two dimensional) materials demonstrate that high T_c superconductors are quite different from the conventional metallic superconductors.⁵⁴⁻⁵⁷ The coherence length (ξ) for $H \parallel c$ is about a factor of 5 larger than when $H \parallel c$.⁵⁸ This anisotropy in ξ means that the properties of any region in the film depend on the orientation of J , H , and the c axis. For example a strong pinning center for $H \parallel c$ may be a region of weak pinning $H \parallel c$. Hence although for $H \parallel c$ and $H \parallel c$ (Figs. 3 and 4) the current flows in the $a-b$ plane, we leave open the possibility that either a pinning or a pair-breaking mechanism operates when $H \parallel c$.

Historically, the compelling experimental evidence that identified the mechanism limiting J_c in metallic/intermetallic superconductors was provided by correlating physical properties with the magnitude of J_c . In systems limited by flux pinning: decoration measurements showed that fluxons were preferentially located on pinning centers^{59,60}; electrical transport measurements demonstrated that J_c increased as the density of flux pinning centers increased.^{61,62} In granular systems, it was shown that the electromagnetic properties were determined by the properties of the barrier.²⁴ We can expect to advance our understanding of the mechanism limiting J_c in epitaxial thin films of high temperature superconductor, when we can correlate the electromagnetic properties with the physical properties.

VI. CONCLUDING COMMENTS

We have measured J_c as a function of magnetic field and temperature on two different films. In these films for $H \parallel c$ we have found that the magnetic field and temperature dependence is consistent with both a flux pinning mechanism and a pair breaking mechanism. In spite of taking data in magnetic fields up to $B_{c2*}(T)$, we cannot distinguish which of these mechanisms operates in this orientation. In contrast, by extending measurements of J_c to very high magnetic fields (~ 27 T) in one of the films, for $H \parallel c$

axis, we have found that J_c is unambiguously exponential of the form $J_c = a(T) \exp[-\mu_0 H/\beta(T)]$. This exponential dependence implies that J_c is not determined by a standard flux pinning mechanism but is instead limited by a pair-breaking mechanism. The standard phenomenological $S-N-S$ junction description is inconsistent with the temperature dependence of this pair-breaking mechanism.

ACKNOWLEDGMENTS

These electromagnetic measurements were made by D. P. H. while he was a post-doctoral research scientist at The Applied Superconductivity Center, Madison Wisconsin. The authors wish to thank Professor D. C. Larbalestier for his considerable contribution to this work. In addition thanks are due to: S. M. Sampere and R. R. Krchnavek for help in preparation of the bridges; and B. Brandt and L. Rubin at the Francis Bitter National Magnet Laboratory, Cambridge, MA for their technical support. The work had the support of the University Funding Council U.K., the Electric Power Research Institute U.S.A. and the Department of Energy and Office of Fusion U.S.A.

¹J. S. Satchell, R. G. Humphreys, N. G. Chew, J. A. Edwards, and M. J. Kane, *Nature* **334**, 331 (1988).
²J. D. Hettinger, A. G. Swanson, W. J. Skocpol, J. S. Brooks, J. M. Graybeal, P. M. Mankiewich, R. E. Howard, B. L. Straughn, and E. G. Burkhardt, *Phys. Rev. Lett.* **62**, 2044 (1989).
³K. Watanabe, H. Yamane, H. Kurosawa, T. Hirai, N. Kobayashi, H. Iwasaki, K. Noto, and Y. Muto, *Appl. Phys. Lett.* **54**, 575 (1989).
⁴T. Hirai and H. Yamane, *J. Cryst. Growth* **107**, 683 (1991).
⁵C. Tome-Rosa, G. Jakob, A. Walkenhorst, M. Maul, M. Schmitt, M. Paulson, and H. Adrian, *Z. Phys. B* **83**, 221 (1991).
⁶B. Roas, L. Schultz, and G. Saemann-Ischenko, *Phys. Rev. Lett.* **64**, 479 (1990).
⁷Y. Kuwasawa, T. Yamaguchi, T. Tosaka, S. Aoki, and S. Nakano, *Physica C* **169**, 39 (1990).
⁸X. G. Qiu, C. G. Cui, S. L. Li, M. X. Liu, J. Li, Y. Z. Zhang, Y. Y. Zhao, P. Xu, L. Li, L. F. Chen, P. F. Chen, N. Li, and G. T. Liu, *J. Appl. Phys.* **70** 2461 (1991).
⁹P. England, T. Venkatesan, X. D. Wu, A. Inam, M. S. Hegde, T. L. Cheeks, and H. G. Craighead, *Appl. Phys. Lett.* **53**, 2336 (1988).
¹⁰S. S. Yom, T. S. Hahn, Y. H. Kim, H. Chu, and S. S. Choi, *Appl. Phys. Lett.* **54** 2370 (1989).
¹¹S.-W. Chan, D. M. Huang, and L. Nazar, *J. Appl. Phys.* **65**, 4719 (1989).
¹²R. F. Kwasnick, F. E. Luborsky, E. L. Hall, M. F. Garbauskas, K. Borst, and M. J. Curran, *J. Mater. Res.* **4**, 257 (1989).
¹³D. P. Hampshire, X. Cai, J. Seuntjens, and D. C. Larbalestier, *Super. Sci. Tech.* **1**, 12 (1988).
¹⁴J. W. Ekin, T. M. Larson, N. F. Bergren, A. J. Nelson, A. B. Swartzlander, L. L. Kazmerski, A. J. Panson, and B. A. Blankenship, *Appl. Phys. Lett.* **52**, 1819 (1988).
¹⁵J. Bardeen and M. J. Stephen, *Phys. Rev. A* **140**, 1197 (1965).
¹⁶S. J. Poon and K. M. Wong, *Phys. Rev. B* **27**, 6985 (1983).
¹⁷L. P. Gorkov and N. B. Kopnin, *Zh. Eksp. Teor. Fiz.* **64**, 356 [Sov. Phys. JETP **37**, 183 (1973)].
¹⁸D. P. Hampshire and H. Jones, *Cryogenics* **27**, 608 (1987).
¹⁹J. Z. Sun, C. B. Eom, B. Lairson, J. C. Bravman, and T. H. Geballe, *Phys. Rev. B* **43**, 3002 (1991).
²⁰W. A. Fietz and W. W. Webb, *Phys. Rev.* **178**, 657 (1969).
²¹E. J. Kramer, *J. Appl. Phys.* **44**, 657 (1969).
²²B. Seeber, C. Rossel, O. Fischer, and W. Glaetze, *IEEE Trans. Magn.* **MAG-21**, 409 (1985).
²³R. G. Hampshire and M. T. Taylor, *J. Phys. F* **2**, 99 (1972).
²⁴P. G. De Gennes, *Rev. Mod. Phys.* **36**, 225 (1964); *Superconductivity of Metals and Alloys* (Benjamin, New York, 1966).
²⁵T. Y. Hsiang and D. K. Finnemore, *Phys. Rev. B* **22**, 154 (1980).
²⁶D. P. Hampshire, J. Seuntjens, L. D. Cooley, and D. C. Larbalestier, *Appl. Phys. Lett.* **53**, 814 (1988).
²⁷L. R. Tessler, J. Provost, and A. Maignan, *Appl. Phys. Lett.* **58**, 528 (1991).
²⁸D. P. Hampshire, A. F. Clark, and H. Jones, *J. Appl. Phys.* **66**, 3160 (1989).
²⁹D. K. Finnemore, J. E. Ostenson, L. Ji, R. W. McCallum, and J. R. Clem, *Adv. Cryo. Eng.* **35**, 613 (1988).
³⁰E. Babic, M. Prester, D. Drobac, Z. Marohnic, and N. Biskup, *Phys. Rev. B* **43**, 1162 (1991).
³¹Y. B. Kim, C. F. Hempstead, and C. F. Strad, *Phys. Rev. A* **139**, 1163 (1965).
³²P. Lebwohl and M. J. Stephen, *Phys. Rev.* **163**, 376 (1967).
³³Z. Liu and G. J. Bowden, *Super. Sci. Tech.* **4**, 122 (1991).
³⁴D. P. Hampshire and H. Jones, *J. Phys. C* **20**, 3533 (1987).
³⁵J. Rosenblatt, P. Peyral, and A. Raboult, in *Inhomogeneous Superconductors* edited by D. U. Gubser, T. L. Francavilla, S. A. Wolf, and J. R. Leibowitz (AIP, New York, 1980), AIP Conf. Proc. Vol. 58, p. 33.
³⁶F. Irie, T. Matsushita, S. Otabe, T. Matsuno, and K. Yamafuji, *Cryogenics* **29**, 317 (1989).
³⁷S. Takacs, P. Polak, and L. Krmpasky, *Cryogenics* **153**, 207 (1983).
³⁸G. Deutscher and K. A. Muller, *Phys. Rev. Lett.* **59**, 1745 (1987).
³⁹J. Bardeen, D. M. Ginsberg, and M. B. Salamon, in *Proceedings of the International Workshop on Novel Mechanisms of Superconductivity*, Berkeley, California, 1987, edited by S. A. Wolf and V. Z. Kresin (Plenum, New York, 1987).
⁴⁰R. J. Cava, A. W. Hewat, E. A. Hewat, B. Batlogg, M. Marezio, K. M. Rabe, J. J. Krajewski, W. F. Peck, Jr., and L. W. Rupp, Jr., *Physica C* **165**, 419 (1990).
⁴¹D. H. Kim, D. J. Miller, J. C. Smith, R. A. Holobow, J. H. Kang, and J. Talvacchio, *Phys. Rev. B* **44**, 7607 (1992).
⁴²P. L. Gammel, D. J. Bishop, G. J. Dolan, J. R. Kwo, C. A. Murray, L. F. Schneemeyer, and J. V. Waszczak, *Phys. Rev. Lett.* **59**, 2592 (1987).
⁴³K. Heine, J. Tenbrink, and M. Thoner, *Appl. Phys. Lett.* **55**, 2441 (1989).
⁴⁴K. Osamura, T. Takayama, and S. Ochiai, *Appl. Phys. Lett.* **55**, 396 (1989).
⁴⁵D. P. Hampshire, J. A. S. Ikeda, and Y. M. Chiang, *Phys. Rev. B* **40**, 8818 (1989).
⁴⁶P. L. Gammel, L. F. Schneemeyer, J. V. Waszczak, and D. J. Bishop, *Phys. Rev. Lett.* **61**, 1666 (1988).
⁴⁷E. H. Brandt, *J. Low Temp. Phys.* **26**, 709 (1977).
⁴⁸E. H. Brandt, *J. Mod. Phys. B* **5**, 751 (1991).
⁴⁹M. Tachiki and S. Takahashi, *Solid State Commun.* **72**, 1083 (1989).
⁵⁰M. V. Feigel'man and V. M. Vinokur, *Phys. Rev. B* **41**, 8986 (1990).
⁵¹P. M. Kes, J. Aarts, I. van der Berg, C. L. van der Beek, and J. A. Mydosh, *Super. Sci. Tech.* **1**, 242 (1989).
⁵²J. van der Berg, C. L. van der Beek, P. M. Kes, J. A. Mydosh, M. J. V. Menken, and A. A. Menovsky, *Super. Sci. Tech.* **1**, 249 (1989).
⁵³Y. Yesurun and A. P. Malozemoff, *Phys. Rev. Lett.* **60**, 2202 (1988).
⁵⁴D. E. Farrell, C. M. Williams, S. A. Wolf, N. P. Bansal, and V. G. Kogan, *Phys. Rev. Lett.* **61**, 2805 (1988).
⁵⁵J. R. Clem, *Phys. Rev. B* **43**, 7837 (1991).
⁵⁶C. A. Bolle, P. L. Gammel, D. G. Grier, C. A. Murray, D. J. Bishop, D. B. Mitzi, and A. Kapitulnik, *Phys. Rev. Lett.* **66**, 112 (1991).
⁵⁷A. I. Buzdin and A. Y. Simonov, *JETP Lett.* **51**, 191 (1990).
⁵⁸U. Welp, W. K. Kwok, G. W. Crabtree, K. G. Vandervoort, and J. Z. Liu, *Phys. Rev. Lett.* **62**, 1908 (1989).
⁵⁹U. Essmann and H. Trauble, *Phys. Lett. A* **24**, 526 (1967).
⁶⁰O. Singh, A. E. Curzon, and C. C. Koch, *J. Phys. D* **9**, 61 (1976).
⁶¹W. Schauer and W. Schelb, *IEEE Trans. Magn.* **MAG-17**, 374 (1981).
⁶²M. Suenaga and A. Ghosh, *IEEE Trans. Magn.* **MAG-21**, 1122 (1985).

JOBNAME: Using JPF1 format PAGE: 1 SESS: 5 OUTPUT: Thu Jan 7 11:57:51 1993

ERRATUM

Erratum: "The critical current density in high fields in epitaxial thin films of $Y_1Ba_2Cu_3O_{7-\delta}$: Flux pinning and pair breaking" [J. Appl. Phys. 72, 1 (1992)]

D. P. Hampshire

Durham University, Department of Physics, South Road, Durham, DH1 3LE, United Kingdom

Siu-Wai Chan

CHI-WEI CHEN
*Columbia University, Henry Krumb School of Mines, Materials Science Division, New York,
New York 10027*

The following sentence should be added to the Acknowledgment section: S.-W. C. acknowledges the support from Air Force Office of Scientific Research, under grant AFOSR F49620-92-J-0160.

Growth of superconducting Y-Ba-Cu-O films on spinel and garnet

Siu-Wai Chan and Manoj Chopra

Columbia University, School of Engineering and Applied Science, Henry Krumb School of Mines, Materials Science Division, New York, New York 10027

Cheng-Chung Chi, Tony Frey, and Chang C. Tsuei
IBM T. J. Watson Research Center, Yorktown Heights, New York 10598

(Received 12 April 1993; accepted for publication 20 September 1993)

Spinel and garnet single crystals of low dielectric constants and loss tangents have been investigated as possible substrate materials for the growth of the Y-Ba-Cu-O superconducting films. In addition to their desirable dielectric properties, these materials are chemically compatible with silicon and compound semiconductors and can be used as the interface materials for the integration of cuprate superconducting films with semiconducting devices. The Y-Ba-Cu-O films grown on (001) $MgAl_2O_4$ and (001) $Y_3Al_5O_{12}$ from a co-evaporation deposition with a subsequent wet anneal exhibit superconductivity with a transition temperature $T_c(R=0)$ of 57 and 74 K, respectively, while strongly (001) textured $YBa_2Cu_3O_{7-x}$ films from the *in situ* laser deposition grown on (001) $MgAl_2O_4$ and (001) $Y_3Al_5O_{12}$ show superconducting transition temperatures $T_c(R=0)$ of 77 and 87 K, respectively. Our work demonstrates that these two materials are viable substrates for the Y-Ba-Cu-O thin films in high frequency device applications.

High temperature superconducting (HTSC) thin films because of their low surface resistance will undoubtedly be applied in high frequency devices operating at microwave, radio, and mm-wave frequencies,¹ but such applications will need substrate materials of low dielectric constants (< 20) and low loss tangents ($< 10^{-3}$). The breakthrough of making high quality HTSC films was originated from the ingenious choice of using strontium titanate ($SrTiO_3$) as the substrate material to provide chemical compatibility and good lattice matching to the superconducting cuprate.² However, strontium titanate ($SrTiO_3$) has too high a dielectric constant (150) and a loss tangent to be useful as substrates for HTSC films in high frequency applications. The search for other perovskite substrates of low dielectric constants and small loss tangent has led to the investigation of substrate materials³ such as $LaAlO_3$ and $LaGaO_3$. However, these perovskites can form surface corrugations from twinning, and thereby limit the superconducting properties of HTSC films grown on them. Other perovskites⁴ have met limited success because large and low dielectric-loss crystals are few due to high growth temperatures and difficulties in controlling stoichiometry.

When the high frequency capability of HTSC is combined with semiconducting devices that operate at GHz frequencies, a new class of devices will appear. Furthermore, there exists for the first time a temperature range within which both semiconductors and superconductors can operate. Between 60 and 80 K, semiconductors will have sufficient non-freezed-out carriers with reasonable mobilities and the cuprate superconductors will superconduct. Undoubtedly, novel devices that combine semiconducting and superconducting materials will impact microelectronics when the integration of existing semiconducting circuits with superconducting thin films is proven to be viable. Successful integration of HTSC films on silicon, III-V and II-VI compound semiconductors require material compatibility. Spinels and garnets are of interest as the

interfacing materials because they have been demonstrated to be chemically and structurally compatible with silicon and compound semiconductors. For example, epitaxial silicon was grown on aluminum spinel ($MgAl_2O_4$)⁵ and $Ga_{0.47}In_{0.53}As-InP$ multilayer quantum wells were grown on (001) gadolinium gallium garnet (GGG).⁶ Besides, there are many spinels and garnets of low dielectric constants (< 20) and of low loss tangents ($< 10^{-3}$), which are important for high frequency applications. Unlike some perovskites, most of the spinels and garnets do not form surface corrugations from twinning and structural phase transformation. There are also wide spectra of lattice parameters to choose from, in the families of spinels and garnets for the least lattice mismatch with superconducting cuprates. When they do melt congruently and below 2000 °C, high quality crystals can be grown by the Czochralski (CZ) method for large substrate applications. Miura *et al.*⁷ used $SrTiO_3/MgAl_2O_4$ as a double buffer layer between Si and YBCO films, while Bansal *et al.*⁸ used $MgAl_2O_4$ as substrates for screen printed thick films. Both groups showed encouraging results. Here, we use the magnesium spinel $MgAl_2O_4$ and yttrium aluminum garnet (YAG) $Y_3Al_5O_{12}$ to explore the feasibility of using them as substrate materials for HTSC thin films.

Two methods are used to deposit the Y-Ba-Cu-O films in order to evaluate the process compatibility of the substrates. The first method, the co-evaporation process, described in detail elsewhere,⁹ is used to grow thin films of Y-Ba-Cu-O onto (001) $MgAl_2O_4$ and (001) $Y_3Al_5O_{12}$ with no buffer layer. Previously, this deposition process has yielded robust $YBa_2Cu_3O_{7-x}$ (YBCO) films on $SrTiO_3$ substrates with some of the highest critical current values.¹⁰ In summary, these films are prepared by the co-evaporation of Y, BaF_2 , and Cu on a substrate held at room temperature. Since the distance between sources and the substrates is 450 mm, films from the same run are of the same composition. The background pressure is

2×10^{-6} Torr and oxygen is introduced with a resulting pressure of 5×10^{-5} Torr during deposition. The use of BaF_2 as barium source provides nonhygroscopic as-deposited films. However, annealing is necessary for the removal of fluorine and the conversion of the as-deposited amorphous materials into the superconducting phase(s).⁶ Subsequent annealing is performed on the as-deposited films both at the standard annealing temperature of 850 °C and at 800 °C.

The second film deposition method is an *in situ* laser deposition process. The operating condition includes a substrate temperature of 740 °C, a pressure of back-filled molecular oxygen at 200 mTorr with a background vacuum at 10^{-6} Torr. The energy density of the excimer laser beam (248 nm) is about 1.5 J/cm^2 per shot and the deposition rate is about 0.05 nm/shot. A stoichiometric $\text{YBa}_2\text{C}_3\text{O}_{7-x}$ pellet is used as the target for the laser ablation. After deposition, the chamber is back filled with 0.5 atm of oxygen with the initial cooling rate maintained at 3 °C/min.

From the coevaporation process, micron thick Y-Ba-Cu-O films grown on (001) yttrium garnet ($\text{Y}_3\text{Al}_5\text{O}_{12}$) and (001) magnesium spinel (MgAl_2O_4) exhibit reasonable superconducting transitions with the complete transition temperatures being 54 and 73 K, respectively. These films are annealed at 800 °C for 30 min. in oxygen with $P_{\text{H}_2\text{O}}$ at 0.7 atm following a standard annealing procedure.⁹ Films from the same deposition run but were annealed at 850 °C with $P_{\text{H}_2\text{O}}$ at 0.02 atm, exhibit similar resistance temperature dependence except with lower total transition temperatures, i.e., 51 and 71 K for films on MgAl_2O_4 and $\text{Y}_3\text{Al}_5\text{O}_{12}$, respectively, possibly because the reaction between films and substrates is accelerated at a higher temperature. As a control, a film on (001) SrTiO_3 from the same run and annealed at 800 °C for 30 min in oxygen with $P_{\text{H}_2\text{O}}$ at 0.7 atm showed a total transition temperature of 79 K, while another control film annealed at the standard temperature of 850 °C with $P_{\text{H}_2\text{O}}$ at 0.02 atm shows a total transition temperature of 85 K. Therefore, the conversion of the as-deposited amorphous materials to superconducting Y-Ba-Cu-O is more complete at 850 °C while at this

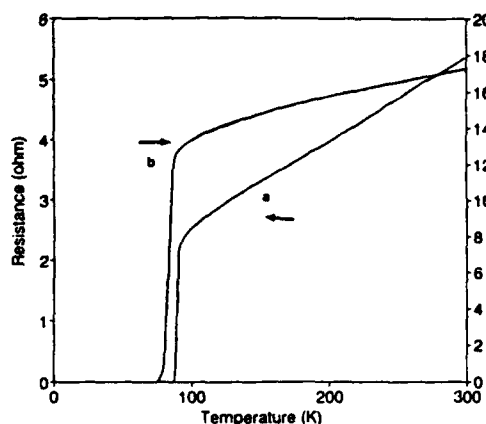


FIG. 1. Resistance-temperature dependence for the $\text{YBa}_2\text{Cu}_3\text{O}_{7-x}$ films deposited on (a) (001) $\text{Y}_3\text{Al}_5\text{O}_{12}$ and (b) (001) MgAl_2O_4 by the *in situ* laser deposition process.

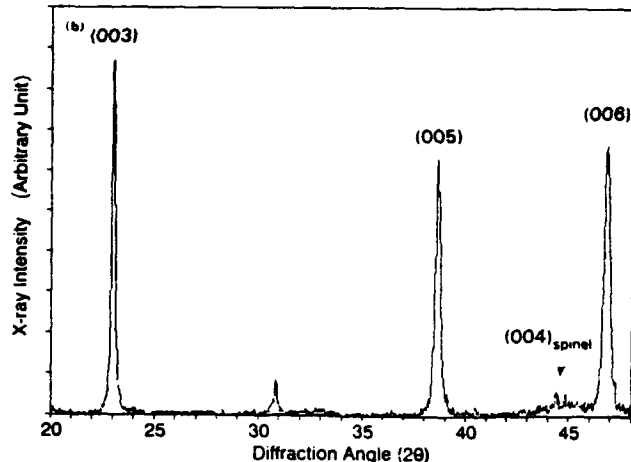
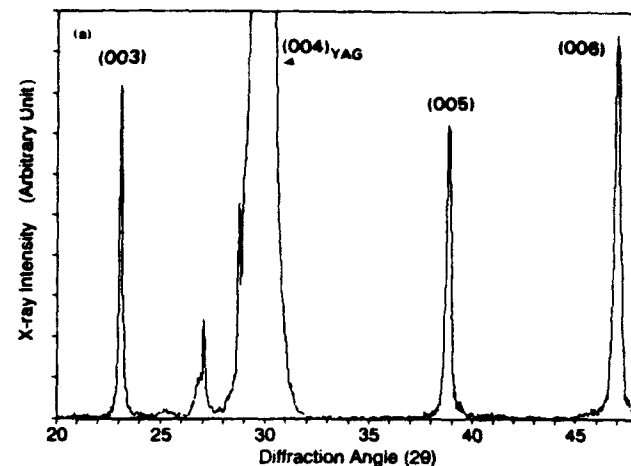


FIG. 2. 2θ scans from x-ray diffraction of the $\text{YBa}_2\text{Cu}_3\text{O}_{7-x}$ films deposited on (a) (001) $\text{Y}_3\text{Al}_5\text{O}_{12}$ and (b) (001) MgAl_2O_4 by the laser deposition. In (a) a much lower incident x-ray intensity is used to scan 2θ from 25° to 35° to avoid the strong diffracted beam from the substrate overloading the detector, while in (b) the spinel substrate is slightly misaligned showing a small (004) spinel peak. The (003), (005), (006), peaks of $\text{YBa}_2\text{Cu}_3\text{O}_{7-x}$ (004)spinel and (004)YAG peaks are labeled.

higher temperature spinel and YAG react more with the films causing some degradation of the superconducting properties of the resulted films. The stoichiometry of these particular as-deposited films from the same run is Cu rich as detected by Rutherford backscattering (RBS) with Y:Ba:Cu ratios being 1:2:4 which can cause the formation of the $\text{Y}_2\text{Ba}_4\text{Cu}_8\text{O}_x$ phase as well as the $\text{YBa}_2\text{Cu}_3\text{O}_{7-x}$ phase. Hence, we call these films Y-Ba-Cu-O films. Indeed, x-ray diffraction of the films shows the (00L) peaks for both phases of comparable intensity and small (103) peaks of the $\text{YBa}_2\text{Cu}_3\text{O}_{7-x}$ phase indicating some randomly orientated grains in the films. The lower transition temperatures in these films are expected since $\text{Y}_2\text{Ba}_4\text{Cu}_8\text{O}_x$ has a lower transition temperature (80 K) than that (90 K) of the $\text{YBa}_2\text{Cu}_3\text{O}_{7-x}$. Besides, the transition of the Y-Ba-Cu-O films on MgAl_2O_4 are broader than those on $\text{Y}_3\text{Al}_5\text{O}_{12}$ for both 800 °C as well as 850 °C anneal, which suggests that MgAl_2O_4 is more reactive than $\text{Y}_3\text{Al}_5\text{O}_{12}$ with the Y-Ba-Cu-O films.

From the laser deposition process, $\text{YBa}_2\text{Cu}_3\text{O}_{7-x}$ (YBCO) films of 200 nm thick show an on-set transition

29/72
TABLE I. Summary of the room temperature properties of magnesium spinel, yttrium aluminum garnet, and strontium titanate: structure, lattice parameters, dielectric constants, maximum temperature as line compounds (T_{\max} 's), and melting temperatures (T_m 's). The last four columns show $T_c(R=0)$ of the deposited films from different processes, and x-ray reflections observed of the $\text{YBa}_2\text{Cu}_3\text{O}_{7-x}$ phase from the laser deposited films. Some of the processing parameters are listed at the bottom two rows of the table.

Substrate material/ chemical formula (all have cubic unit cells)	Lattice parameter (nm)	T_{\max} Maximum temp. of the line compound	Dielectric constant ^c at 9.1 GHz	$T_c(R=0)$ of the films from the co-evaporation process (K)	$T_c(R=0)$ of the laser deposited films (K)	X-ray reflections of the laser deposited films	
Magnesium spinel	MgAl_2O_4	0.8083	800 °C ($T_m=2105$ °C) ^a	12	51	57	77 (003), (005), (006)
YAG Yttrium Aluminum Garnet	$\text{Y}_3\text{Al}_5\text{O}_1$	1.2009	1970 °C ^b	10	71	74	87 (003), (005), (006)
Strontium titanate	SrTiO_3	0.3905	($T_m=2000$ °C) ^c	150 (zero frequency)	85	79	89
Processing parameters		Annealing/substrate temp. (°C) Partial pressure of H_2O in atm		850 0.02	800 0.7	740 not applicable	

^aReference 11.

^bReference 12.

^cReference 4.

temperature (T_{on}) of 91 K with a total transition temperature $T_c(R=0)$ of 87 K when grown on (001) YAG and an on-set at 87 K with $T_c(R=0)=77$ K for the film on (001) MgAl_2O_4 (Fig. 1). The normal resistivities of these films are 160 and 490 $\mu\Omega\text{ cm}$ at room temperature. X-ray diffraction (Fig. 2) shows strong (003), (005), and (006) reflections of $\text{YBa}_2\text{Cu}_3\text{O}_{7-x}$ phase from both films indicating a good plane alignment of (001)_{film} || (001)_{substrate}, while no $\text{Y}_2\text{Ba}_4\text{Cu}_8\text{O}_x$ phase is detected.

From these results, it is obvious that the YAG substrates are much better substrates than the spinel ones, disregarding which of the two deposition methods used. Both MgAl_2O_4 and $\text{Y}_3\text{Al}_5\text{O}_1$ exist as line compounds in the corresponding phase diagrams of the pseudobinary oxide systems of $\text{Al}_2\text{O}_3\text{-MgO}$ ¹¹ and $\text{Y}_2\text{O}_3\text{-Al}_2\text{O}_3$,¹² respectively. However, MgAl_2O_4 deviates from a line compound to form a solid solution at about 800 °C, whereas $\text{Y}_3\text{Al}_5\text{O}_1$ remains as a line compound up to 1970 °C showing a higher phase stability than the spinel, which can also explain the higher reactivity of MgAl_2O_4 with the Y-Ba-Cu-O films. For low reactivity with films, substrate materials need to exhibit phase stability at a temperature significantly higher than both the deposition and the annealing temperature used during film processing. Therefore, the maximum line-compound temperature of a substrate material can be a good indicator of the reactivity with films for future selection of possible substrates.

In summary, we have successfully grown superconducting Y-Ba-Cu-O films on (001) MgAl_2O_4 and on (001) $\text{Y}_3\text{Al}_5\text{O}_1$ both by the *in situ* laser deposition and by the co-evaporation with a follow-up anneal. The best result is the $\text{YBa}_2\text{Cu}_3\text{O}_{7-x}$ films deposited by *in situ* laser deposition on (001) $\text{Y}_3\text{Al}_5\text{O}_1$ (YAG) which exhibits (001) plane alignment between the films and the substrates. Possible epitaxy relation is being investigated using transmission electron microscopy. Important data about substrates and results of the deposited Y-Ba-Cu-O films are summarized in Table I. We find that the best quality films can be

grown on (001) YAG while YAG has low radio frequency losses and a low dielectric constant with no surface corrugation problem. The next challenge will be to show both semiconducting devices and cuprate superconducting elements on the same YAG substrate.

S.-W. C. and M. C. acknowledge the support from the Air Force Office of Scientific Research, under Grant AFOSR F49620-92-J-0160. S.-W. C. would like to thank P. L. Key for the permission to use the x-ray diffractometer, and B. J. Wilkins for the RBS analysis.

^aW. Hartwig and C. Passow, in *Applied Superconductivity*, edited by V. L. Newhouse (Academic, New York, 1975), Vol. II, p. 542.

^bP. Chaudhari, R. H. Koch, R. B. Laibowitz, T. R. McQuire, and R. J. Gambino, *Phys. Rev. Lett.* **58**, 2684 (1987).

^cR. W. Simon, C. E. Platt, A. E. Lee, G. S. Lee, K. P. Daly, M. S. Wire, J. A. Luine, and Urbanik, *Appl. Phys. Lett.* **53**, 2677 (1988); G. Koren, A. Gupta, E. A. Giess, A. Segmuller, and R. B. Laibowitz, *ibid.* **54**, 1054 (1989).

¹R. I. Belf and R. Uhrin, *The Proceeding of Science and Technology of Superconducting Thin Films* (Plenum, New York 1989).

²S. H. McFarland and C. C. Wang, *J. Appl. Phys.* **43**, 1724 (1972).

³M. Razeghi, P.-L. Meunier, and P. Maurel, *J. Appl. Phys.* **59**, 2261 (1986).

⁴S. Miura, T. Toshitake, S. Matsubara, Y. Miyasaka, N. Shohata, and T. Satoh, *Appl. Phys. Lett.* **53**, 1967 (1988).

⁵N. P. Bansal and R. N. Simon, *Appl. Phys. Lett.* **53**, 603 (1988).

⁶Siu-Wai Chan, B. G. Bagley, L. H. Greene, M. Giroud, W. L. Feldmann, K. R. Jenkin II, and B. J. Wilkins, *Appl. Phys. Lett.* **53**, 1443 (1988).

⁷P. M. Mankiewich, R. E. Howard, W. J. Skocpol, A. H. Dayem, A. Ourmazd, M. G. Young, and E. Good, *Mater. Res. Soc. Symp.* **99**, 119 (1988).

⁸A. M. Alper, R. N. McNally, P. G. Ribbe, and R. C. Doman, *J. Am. Ceram. Soc.* **45**, 264 (1962); D. M. Roy, R. Roy, and E. F. Osborn, *ibid.* **36**, 149 (1953).

⁹I. Warshaw and R. Roy, *J. Am. Ceram. Soc.* **42**, 435 (1959); S. J. Schneider, R. S. Roth, and J. L. Waring, *J. Res. Natl. Bur. Stand.* **65**, 364 (1961).